



**HAL**  
open science

# Observed Subcloud-Layer Moisture and Heat Budgets in the Trades

Anna Lea Albright, Sandrine Bony, Bjorn Stevens, Raphaela Vogel

► **To cite this version:**

Anna Lea Albright, Sandrine Bony, Bjorn Stevens, Raphaela Vogel. Observed Subcloud-Layer Moisture and Heat Budgets in the Trades. *Journal of the Atmospheric Sciences*, 2022, 79 (9), pp.2363-2385. 10.1175/JAS-D-21-0337.1 . hal-03787206

**HAL Id: hal-03787206**

**<https://hal.sorbonne-universite.fr/hal-03787206v1>**

Submitted on 21 Mar 2023

**HAL** is a multi-disciplinary open access archive for the deposit and dissemination of scientific research documents, whether they are published or not. The documents may come from teaching and research institutions in France or abroad, or from public or private research centers.

L'archive ouverte pluridisciplinaire **HAL**, est destinée au dépôt et à la diffusion de documents scientifiques de niveau recherche, publiés ou non, émanant des établissements d'enseignement et de recherche français ou étrangers, des laboratoires publics ou privés.

## Observed Subcloud-Layer Moisture and Heat Budgets in the Trades

ANNA LEA ALBRIGHT,<sup>a</sup> SANDRINE BONY,<sup>a</sup> BJORN STEVENS,<sup>b</sup> AND RAPHAELA VOGEL<sup>a</sup>

<sup>a</sup> *Laboratoire de Météorologie Dynamique, CNRS, Sorbonne Université, Ecole Normale Supérieure, Ecole Polytechnique, Paris, France*

<sup>b</sup> *Max Planck Institute for Meteorology, Hamburg, Germany*

(Manuscript received 4 January 2022, in final form 3 May 2022)

**ABSTRACT:** The trade wind subcloud layer is an important structural component of the atmosphere. Its thermodynamic variability has long been characterized using simple frameworks, of which mixed-layer theory is the simplest kind. Past studies qualitatively support such a description, yet the adequacy of mixed-layer theory as a quantitative description has not been tested. Here we use observations collected during the Elucidating the Role of Clouds–Circulation Coupling in Climate (EUREC<sup>4</sup>A) field campaign to test this framework and evaluate our understanding of the trade wind subcloud layer. We find evidence for a transition layer separating the mixed-layer and subcloud-layer tops. The presence of such a finitely thick transition layer with vertical gradients complicates the application of mixed-layer theory, which assumes an abrupt gradient, or “jump” at the subcloud-layer top. This ambiguity introduces effective parameters and motivates their estimation through a Bayesian methodology. Results from this Bayesian inversion further reflect a finite-depth entrainment zone. We find that subcloud-layer moisture and heat budgets close for synoptic variability and a monthly campaign mean, yielding a campaign-mean residual of  $3.6 \text{ W m}^{-2}$  for moisture and  $2.9 \text{ W m}^{-2}$  for heat. Surface wind speed variability influences the subcloud-layer depth and fluxes, yet thermodynamic variability above the subcloud-layer top emerges as the primary control on subcloud-layer moisture and heat variability. Given that this simple theoretical framework can explain observed variability, it offers an appealing framework for evaluating larger-scale models that must parameterize the processes regulating this fundamental part of the atmosphere.

**KEYWORDS:** Marine boundary layer; Heat budgets/fluxes; Surface fluxes; In situ atmospheric observations; Bayesian methods; Idealized models; Atmosphere; Atlantic Ocean; Field experiments; Wind effects; Buoyancy; Boundary layer


### 1. Introduction

The trade wind subcloud layer is an important component of the tropical atmosphere. Typically defined as extending from the top of the surface layer (at approximately 50 m) to cloud base (e.g., Malkus 1958; Stevens et al. 2017), it couples the surface to the trade wind cloud layer and, in so doing, regulates the import of heat and moisture from the ocean to the atmosphere above (e.g., Malkus 1958; LeMone and Pennell 1976; Stevens 2007). Clouds are influenced by subcloud-layer properties, as subcloud moisture variability controls moist static energy variability, which influences convective potential and cloudiness (e.g., Emanuel 1986, 1993). Clouds also influence the subcloud layer, as they introduce variability in surface fluxes and radiation, influence wind shear, and mix down dry air from aloft that can then be entrained into the subcloud layer (e.g., Stevens 2006). This subtle interplay between the subcloud and cloud layers ultimately governs the magnitude of latent heat transport from the trades to the equator (e.g., Malkus 1958). The trade

wind subcloud layer thus forms an important link in the global thermodynamic budget, transporting latent heat to the equatorial belt where it influences large-scale circulations and the global hydrological cycle (Riehl 1954; Heckley 1985; Tiedtke 1989).

To the extent that the subcloud layer influences the cloud layer, the clouds of the trades provide an additional motivation to study the trade wind subcloud layer. By virtue of their large spatial extent and thus statistical weight, trade wind cloud regimes have a large influence on the global energy budget and global dynamics (e.g., Bony et al. 2004). Differences in the response of trade wind cumulus to warming explain large differences in climate sensitivity estimates (e.g., Bony and Dufresne 2005; Webb et al. 2006; Vial et al. 2013; Myers et al. 2021), some of which have been shown to relate to how efficiently moisture is exported out of the trade wind subcloud layer (Sherwood et al. 2014).

Given the importance of the trade wind subcloud layer, it is useful to understand what controls its properties. To aid this understanding, the subcloud layer has long been characterized using simple frameworks. Turbulence is expected to homogenize subcloud-layer thermodynamic variables in the vertical (e.g., Mahrt 1976; Stull 2012). Such a well-mixed vertical structure allows for simplification by solving for the vertically integrated, or bulk, properties of the subcloud layer. Among these the vertically integrated, or bulk models, the mixed-layer model is the simplest case, representing the subcloud layer by a single vertically averaged value. As reviewed by Stevens (2006), mixed-layer models have formed a basis for representing the subcloud layer in larger-scale models (Deardorff 1972; Arakawa and Schubert

 Denotes content that is immediately available upon publication as open access.

Vogel's current affiliation: University of Hamburg, Hamburg, Germany.

*Corresponding author:* Anna Lea Albright, anna-lea.albright@lmd.ipsl.fr

DOI: 10.1175/JAS-D-21-0337.1

© 2022 American Meteorological Society. For information regarding reuse of this content and general copyright information, consult the [AMS Copyright Policy](#) ([www.ametsoc.org/PUBSReuseLicenses](http://www.ametsoc.org/PUBSReuseLicenses)).

1974), thermodynamic models of the tropics (Betts and Ridgway 1989; Miller 1997), diagnostic studies of surface winds over tropical oceans (Stevens et al. 2002; McGauley et al. 2004), and diagnostic studies of specific regions, including trade wind regimes (Betts 1976; Betts and Albrecht 1987; Neggers et al. 2006), deep convective regions (Emanuel 1993; Raymond 1995), or stratocumulus regimes (Kraus 1963; Lilly 1968; Wood and Bretherton 2004). Mixed-layer models allow for quantifying the magnitude of different processes that control subcloud-layer variability and attributing this variability to changes in the environment.

The adequacy of this mixed-layer description of the subcloud layer has, however, only been assessed from relatively few measurements and large-eddy simulations often performed for idealized conditions over small (and usually homogeneous) domains. Past observational studies typically used approximately 100 dropsondes and fixed certain parameters, such as the sea surface temperature and vertical thermodynamic structure above the subcloud layer (Betts 1976; Betts and Albrecht 1987; Betts and Ridgway 1989). Other studies examining large-scale heat and moisture budgets (Augstein et al. 1973; Yanai et al. 1973; Holland and Rasmusson 1973; Nitta and Esbensen 1974) considered the layer up to the trade wind inversion, therefore focusing on different vertical transports than our budgets for the subcloud layer. Augmenting subcloud-layer thermodynamic analyses with passive remote sensing remains challenging, in particular regarding the boundary layer height, entrainment flux, and vertical motions (e.g., Kalmus et al. 2014). Indeed, tropical moisture variability is poorly quantified by passive remote sensing, especially in the lowest three kilometers, because observed moisture profile features are at scales much finer than the typical weighting functions of even hyperspectral instruments (e.g., Maddy and Barnet 2008; Chazette et al. 2014; Stevens et al. 2017; Pincus et al. 2017). Output from large-eddy simulations could, conceivably, be used to evaluate mixed-layer theory, and mixed-layer models have been used to interpret large-eddy simulations (e.g., Neggers et al. 2006; Bellon and Stevens 2012, 2013; Schalkwijk et al. 2013). Indeed, the apparent realism of large-eddy simulations can suggest a trustworthy representation of nature, yet these simulations use idealized boundary conditions, employ a range of domain sizes and resolutions, and rarely represent the diversity of mesoscale patterns of convection observed in nature, all of which introduce uncertainty into the resultant thermodynamic fields (e.g., Bony et al. 2017). The limitations of both passive remote sensing and large-eddy simulation output render in situ observations especially important for testing mixed-layer theory as a description of the trade wind subcloud layer.

As part of the Elucidating the Role of Clouds–Circulation Coupling in Climate (EUREC<sup>4</sup>A) field campaign (Bony et al. 2017; Stevens et al. 2021), we collected the necessary data to investigate the structure and variability of the trade wind subcloud layer. These data allow us to test whether mixed-layer theory is a reasonable and useful theoretical framework for studying the trade wind subcloud layer. After verifying that the assumptions of mixed-layer theory are reasonable relative to observational constraints, we test whether this simple framework is useful for diagnosing the balance of physical processes controlling subcloud-layer thermodynamic variability and its large-scale

environmental controls. A primary motivation for the EUREC<sup>4</sup>A campaign was to make the first process-based constraint on the trade cumulus feedback, which is undertaken in Vogel et al. (2022, manuscript submitted to *Nature*). The process-based approach in Vogel et al. (2022, manuscript submitted to *Nature*) makes use of the mixed-layer framework, albeit for the subcloud-layer mass budget. Another motivation for the present paper is therefore to evaluate the adequacy of the mixed-layer framework for subcloud-layer moisture and heat, in order to assess whether it can be applied to the subcloud-layer mass budget and thus the evaluation of trade cumulus feedbacks.

To this end, section 2 presents the EUREC<sup>4</sup>A observations, and section 3 defines subcloud-layer variability in terms of five parameters—its height, as well as its means and gradients in specific humidity and potential temperature—and quantifies how each parameter contributes to variability across measurement periods separated by hours to weeks. Section 4 introduces the mixed-layer theory framework and a Bayesian methodology that is used to jointly constrain uncertain parameters related to entrainment. Section 5 then evaluates whether this simple theoretical framework, applied to in situ observations, can explain observed synoptic variability and the monthly campaign-mean for moisture and heat. Section 6 examines the relationships among subcloud-layer properties and large-scale meteorological conditions, and section 7 presents discussion and conclusions.

## 2. EUREC<sup>4</sup>A field campaign data

EUREC<sup>4</sup>A field study measurements were made in January and February 2020 in the North Atlantic trade wind regions, east of Barbados, to study the couplings among clouds, circulations, and their large-scale environment. In both models and observations, clouds and the large-scale environment around Barbados were found to be representative of the Atlantic and Pacific trades (Medeiros and Nuijens 2016; Rasp et al. 2020), suggesting that many inferences from EUREC<sup>4</sup>A observations are informative of trade wind regions globally. EUREC<sup>4</sup>A sets itself apart from previous field campaign that are, for instance, reviewed by Garstang et al. (2019), through the intense and unbiased sampling; the use of novel observing strategies combined with improved and novel instrumentation; and the coincidence of satellite measurements with very high spatial resolution and temporal sampling (Bony et al. 2017; Stevens et al. 2021).

Figure 1 shows the geographic distribution of the measurements used in this study. Our core data are 810 dropsondes from the German High Altitude and Long Range Research Aircraft (HALO) launched between 22 January and 15 February 2020 (George et al. 2021; Konow et al. 2021). These dropsondes yield vertical profiles of pressure, temperature, and relative humidity with a manufacturer-stated accuracy of 0.4 hPa, 0.1°C, and 2%, respectively (Vaisala 2022). We employ level-3 and level-4 dropsonde data, which have been processed and interpolated into a common altitude grid with 10 m vertical resolution (George et al. 2021). We note that George et al. (2021) identify a dry bias in the HALO dropsondes, which they correct with a multiplicative factor of 1.06 applied to relative humidity and all associated moisture quantities from these sondes. We use these corrected data.

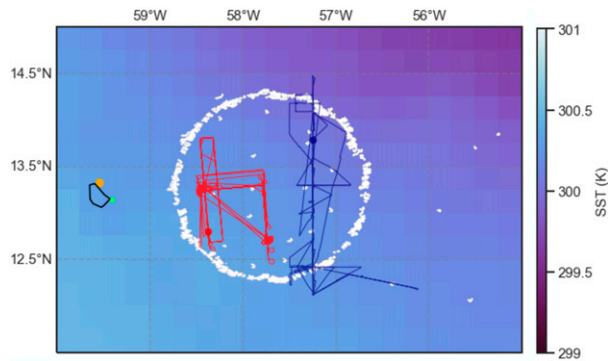


FIG. 1. Data employed in this study include dropsondes launched in the EUREC<sup>4</sup>A circle (white; 810 HALO dropsonde soundings), subcloud-layer thermodynamic measurements from the ATR-42 aircraft (red tracks), and sea surface temperature and surface flux measurements from the R/V *Meteor* (navy tracks). We also use data from the Barbados Cloud Observatory (green) and subcloud-layer thermodynamic measurements from the remotely piloted aircraft CU-RAAVEN (orange). For illustrative purposes, background sea surface temperatures are ERA5 data at 0.25° resolution, averaged over January and February 2020.

One unique aspect of EUREC<sup>4</sup>A is the sampling strategy that provides aggregated, statistical estimates of a larger-scale signal, compared to individual point-wise measurements. During EUREC<sup>4</sup>A, dropsonde measurements were distributed along a fixed flight pattern, the “EUREC<sup>4</sup>A circle”—the EUREC<sup>4</sup>A circle is a circular flight pattern with an approximately 220-km diameter, centered at 13.3°N, 57.7°W, and at 9.5 km altitude (Fig. 1). The spatial scale of the EUREC<sup>4</sup>A circle characterizes the large-scale environment and corresponds to the size of a typical general circulation model grid box, or what [Orlanski \(1975\)](#) called the meso- $\beta$  scale (20–200 km). Given that measurements did not target specific meteorological conditions (e.g., no “cloud-chasing”), they provide unbiased sampling of the large-scale environment.

Following [Stevens et al. \(2021\)](#), one *circle-mean* refers to the mean of typically 12 dropsondes launched over 1 h along the EUREC<sup>4</sup>A circle (due to operator and instrument errors, on some circles fewer sondes were launched, but never fewer than seven). A dropsonde is launched for every 30° change in heading. Typically each flight incorporated two—temporally well separated—periods of “circling.” A *circling-mean* is defined as the mean of three consecutive circle-means (or in two cases, two circle-means), corresponding to 30–36 consecutive soundings aggregated over 210 min. Variability on the circling-mean scale captures how the large-scale environment varies across about 3.5-hourly periods, and we refer to variability measured on the circling-mean scale as synoptic variability. The *campaign-mean* refers to the mean of 810 dropsondes launched from the HALO aircraft between 22 January and 15 February 2020, or approximately a monthly mean. In total, the dropsonde data are aggregated to 69 circle-means, 24 circling-means, and 1 campaign-mean.

The French ATR-42 aircraft made thermodynamic measurements during 18 flights from 26 January to 13 February 2020.

The ATR-42 flew coincident rectangular patterns inside the EUREC<sup>4</sup>A circle (see Fig. 1), therefore also providing unbiased measurements of the large-scale environment. Its thermodynamic measurements show good agreement with the HALO dropsonde measurements ([Bony et al. 2022](#)). We also make use of smaller-scale thermodynamic measurements between 24 January and 15 February 2020 below 1 km from a remotely piloted aircraft CU-RAAVEN ([de Boer et al. 2022](#)). Sea surface temperatures are from the R/V *Meteor*, with these values extrapolated from the R/V *Meteor* location to the respective dropsonde location based on fixed zonal and meridional sea surface temperature gradients of  $-0.14 \text{ K degree}^{-1}$  of latitude or longitude ([Vogel et al. \(2022, manuscript submitted to Nature\)](#)). These gradients are estimated from two satellite products (*GOES-16* ABI and CLS) and ECMWF Reanalysis of Meteorological data (ERA5, [Hersbach et al. 2020](#)), which agree well over the same spatiotemporal domain. To a lesser extent and solely for purposes of comparison with our observations, we use ERA5 data at 0.25° spatial and hourly temporal resolution for January and February 2020, for surface sensible and latent heat fluxes and vertical profiles of specific humidity and potential temperature.

### 3. Describing the subcloud-layer structure and its variability

To conceptualize the subcloud layer we first consider a representation in terms of five scalar variables: height or depth ( $h$ ), mean potential temperature ( $\bar{\theta}$ ), mean specific humidity ( $\bar{q}$ ), as well as vertical gradients in potential temperature ( $\partial\theta/\partial z$ ) and specific humidity ( $\partial q/\partial z$ ). We hypothesize that knowing these five variables is sufficient to characterize the subcloud layer and how it varies thermodynamically.

#### a. Defining the subcloud-layer height

We first ask to what extent the subcloud-layer height  $h$  can be defined from observed thermodynamic profiles. Despite its role as a key vertical length scale, there is no consensus on how to define this height (e.g., [Seibert et al. 2000](#)). Different methods applied to a single dataset have been shown to yield a wide range of heights (e.g., [Liu and Liang 2010](#); [Beyrich and Leps 2012](#); [Dai et al. 2014](#)), leading to ambiguity in the fundamental question of the depth of the trade wind subcloud layer.

To estimate  $h$ , we use three subcloud height methods, as described here and in greater detail in [appendix A](#). Results are summarized in [Table 1](#). The first method estimates the depth over which there is no vertical gradient in a conserved variable within a threshold following [Canut et al. \(2012\)](#). This “gradient method” selects the height where a thermodynamic variable exceeds its mean, averaged over the levels below, by a certain threshold  $\epsilon$ —that is, that height at which the variable is no longer well-mixed vertically. For instance, for specific humidity, the depth is chosen where  $|q(z) - \bar{q}_\rho| \leq \epsilon_q$ , where  $\bar{q}_\rho = (1/z) \int_{100}^z q(z) dz$  is updated at each vertical level and computed as the density-weighted mean from 100 m to a depth  $z$ . We apply this method to  $q$ ,  $\theta$ , and virtual potential temperature  $\theta_v$ , a proxy for buoyancy. Empirically, we choose



TABLE 1. Campaign-mean and standard deviation of different terms as calculated from the 24 circling-mean data (3-hourly time scale) located in the “EUREC<sup>4</sup>A circle.” Various heights are given:  $h(\text{ML})$  is the mixed-layer top height,  $h(\text{SC})$  is the subcloud-layer top height,  $h(\text{LCL})$  is the lifting condensation level, and  $\Delta h(\text{TL})$  is the thickness of the transition layer, defined as the difference between the subcloud-layer and mixed-layer tops. The subscript  $s$  refers to the surface, and “ML” and “SC” refer to the mixed layer and subcloud layer, respectively. The sea surface temperature (SST) values include the cool-skin approximation adjustment; that is, they include the 0.25 K subtracted from R/V *Meteor* SSTs.  $\|U\|$  refers to the wind speed at 10 m. Vertical gradients are expressed per kilometer.

|                                     | Units                              | Mean  | St dev |
|-------------------------------------|------------------------------------|-------|--------|
| $h(\text{ML})$                      | m                                  | 555   | 79.0   |
| $h(\text{SC})$                      | m                                  | 708   | 83.6   |
| $h(\text{LCL})$                     | m                                  | 694   | 105    |
| $\Delta h(\text{TL})$               | m                                  | 152   | 50     |
| $q_s$                               | $\text{g kg}^{-1}$                 | 22.59 | 0.189  |
| $\bar{q}_{\text{ML}}$               | $\text{g kg}^{-1}$                 | 15.3  | 0.886  |
| $\bar{q}_{\text{SC}}$               | $\text{g kg}^{-1}$                 | 15.1  | 0.883  |
| SST                                 | K                                  | 300.0 | 0.169  |
| $\theta_s$                          | K                                  | 299.2 | 0.260  |
| $\bar{\theta}_{\text{ML}}$          | K                                  | 298.3 | 0.235  |
| $\bar{\theta}_{\text{SC}}$          | K                                  | 298.4 | 0.253  |
| $\ U\ $                             | $\text{m s}^{-1}$                  | 8.46  | 2.19   |
| $\partial q/\partial z$ (ML)        | $\text{g kg}^{-1} \text{ km}^{-1}$ | -1.06 | 0.293  |
| $\partial q/\partial z$ (TL)        | $\text{g kg}^{-1} \text{ km}^{-1}$ | -6.69 | 2.11   |
| $\partial \theta/\partial z$ (ML)   | $\text{K km}^{-1}$                 | 0.424 | 0.291  |
| $\partial \theta/\partial z$ (TL)   | $\text{K km}^{-1}$                 | 2.49  | 0.644  |
| $\partial \theta_v/\partial z$ (ML) | $\text{K km}^{-1}$                 | 0.233 | 0.247  |
| $\partial \theta_v/\partial z$ (TL) | $\text{K km}^{-1}$                 | 1.30  | 0.324  |

a threshold  $\epsilon$  that is one-third of small-scale variability, estimated as within-day variability from 50 to 550 m depth. These threshold values for  $q$ ,  $\theta$ , and  $\theta_v$  are  $0.35 \text{ g kg}^{-1}$ ,  $0.15$  and  $0.20 \text{ K}$ , respectively. The second method, following [Holzworth \(1964\)](#), estimates the level at which a hypothetical rising parcel of near-surface air, representing a thermal, reaches its level of neutral buoyancy, based on a cloud-layer  $\theta_v$  profile, without any overshoot. The third definition finds the peak in the relative humidity profile, given that relative humidity is expected to maximize at the subcloud-layer top if specific humidity is constant and temperature decreases with height.

From this analysis, a conceptual picture emerges of two distinct vertical layers. The first layer is a well-mixed layer in  $q$  and  $\theta$  ([Fig. 2](#), [Fig. B1](#)), which also corresponds to the distribution of relative humidity maxima. Averaging these three height methods gives a mean depth of 555 m ([Figs. 2a,c](#)). A layer that is well-mixed vertically in  $q$  and  $\theta$  has previously been called the mixed-layer (e.g., [Malkus 1958](#); [Augstein et al. 1974](#)), and we adopt this same terminology. The buoyancy variable,  $\theta_v$ , however, remains better-mixed over a deeper layer, to a mean depth of 708 m averaged between the  $\theta_v$ -gradient and parcel methods. Such a layer that is better-mixed deeper in  $\theta_v$  than  $q$  and  $\theta$  individually was observed previously (e.g., [Malkus 1958](#); [Augstein et al. 1974](#);

[Nicholls and Lemone 1980](#); [Yin and Albrecht 2000](#)). This depth also coincides with the mean lifting condensation level (LCL) of 708 m. Each LCL value is the mean of LCL values calculated for air masses from 50 to 300 m. Note that the LCL is calculated from circle- or circling-mean air, which averages subcloud-layer air from areas that are in regions of clear skies and in regions where clouds form above. If the LCL is, however, calculated from individual dropsonde soundings, the distribution shifts lower, with the moistest parcels having LCL values that align with the mixed-layer top (not shown). Historically, the layer that is better-mixed in  $\theta_v$  and corresponds to the environmental-mean cloud base or LCL level is often called the subcloud layer (e.g., [Malkus 1958](#); [Augstein et al. 1974](#); [Nicholls and Lemone 1980](#); [Yin and Albrecht 2000](#)). Although this naming can be confusing, because clouds already start to form *below* the subcloud-layer top, we retain this terminology. This height analysis suggests that there is some ambiguity in the determination of the boundary layer depth.

We associate this ambiguous region between the mixed-layer top and subcloud-layer top with the transition layer ([Malkus 1958](#)). Such a layer is often found in observations ([Augstein et al. 1974](#); [Yin and Albrecht 2000](#)), is used in simple theoretical modeling approaches (e.g., [Albrecht et al. 1979](#)), and emerges in simulations ([Stevens et al. 2001](#)), yet the processes that give rise to its structure remain little investigated. Here defined as the difference between the subcloud-layer top ( $\theta_v$ -gradient method) and mixed-layer top ( $q$ -gradient method), the transition layer has thickness  $151 \pm 77 \text{ m}$  in circle-mean data and  $152 \pm 50 \text{ m}$  in circling-mean data. The mixed-layer top and subcloud-layer top heights, moreover, vary coherently, with a Pearson correlation coefficient of  $r = 0.86$ . Over this interfacial transition layer,  $q$  and  $\theta$  begin to exhibit vertical gradients, albeit in ways that have compensating effects on buoyancy, so that  $\theta_v$  gradients are less pronounced (e.g., [Nicholls and Lemone 1980](#); [Betts and Albrecht 1987](#); [Yin and Albrecht 2000](#)), as illustrated schematically in [Fig. 2b](#)). The differing vertical structures of the mixed layer and transition layer suggests that they may be controlled by different physical processes, which is the subject of a future study ([Albright et al. 2022](#), manuscript submitted to *J. Atmos. Sci.*).

In simple modeling studies, an interpretation arose that the transition layer could be modeled as an infinitely thin layer with “jumps,” or abrupt discontinuities, in analogy with the cloud-free convective boundary layer (e.g., [Lilly 1968](#); [Tennekes 1973](#); [Arakawa and Schubert 1974](#); [Albrecht et al. 1979](#); [Stevens 2006](#)). EUREC<sup>4</sup>A measurements do not, however, show the subcloud layer to be a layer defined by a sharp jump or discontinuity at its top, either in aggregated soundings ([Fig. 2c](#)) or most individual soundings (see one example in [Fig. 2d](#)). Rarely, in about 10% of cases, a profile with a sharp jump occurs, such as shown in [Fig. 2d](#). The presence of such sharp discontinuities, if rare, does, however, show that smoother profiles are not an artifact of potentially slow dropsonde moisture sensor time responses, and they are instead a physical feature of the atmosphere. The ability of the sondes to measure such sharp profiles is consistent with the manufacturer-stated sensitivities for the Vaisala dropsonde RD41, which have a temperature response time of 0.5 s and moisture response time of less than 0.3 s at 1000 hPa, 20°C, and the fall speed of the sonde (roughly  $6.5 \text{ m s}^{-1}$ ) ([Vaisala 2022](#)). Indeed, [Vömel et al. \(2021\)](#) show that the new

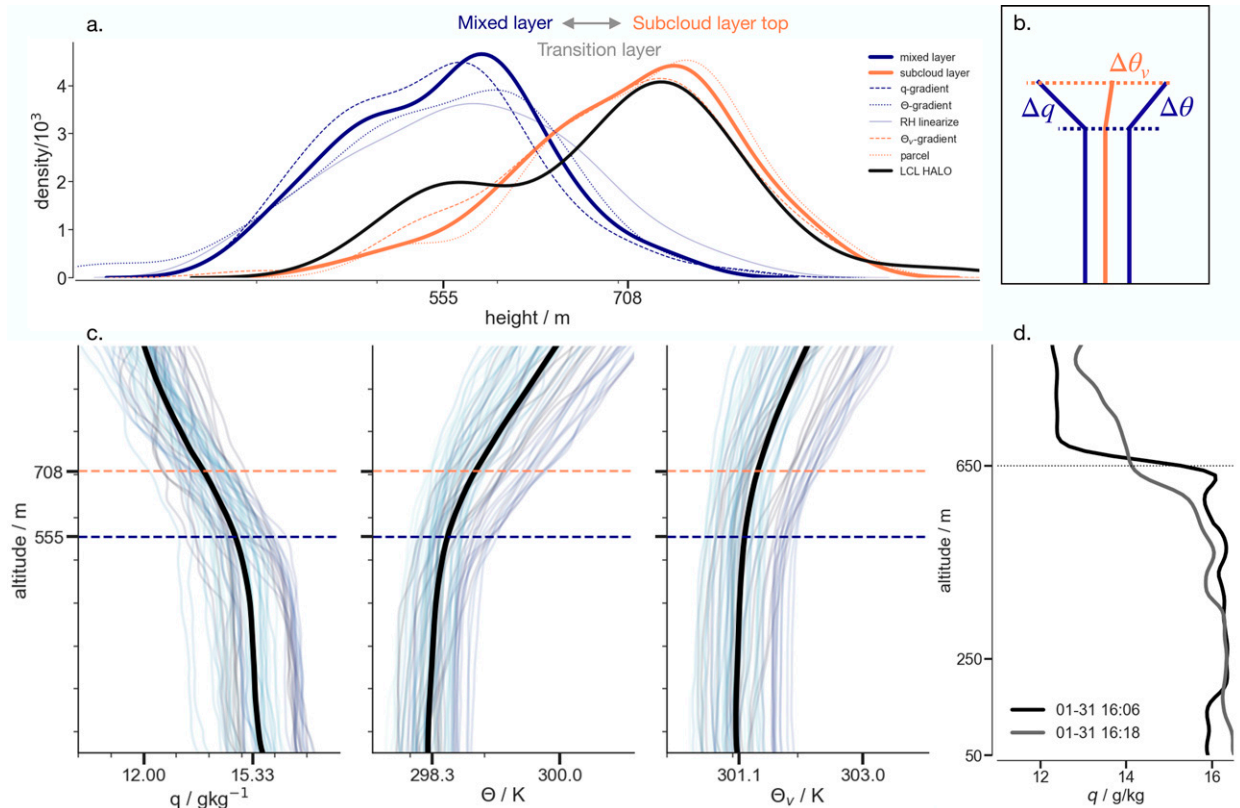


FIG. 2. (a) Probability distributions from different methods employed to estimate the mixed and subcloud-layer heights. We find that three methods based on specific humidity  $q$  or potential temperature  $\theta$  and relative humidity (blue curves) correspond to the mixed-layer top. Two methods using virtual potential temperature  $\theta_v$  (the  $\theta_v$ -gradient method and parcel method; orange profiles) instead correspond to a deeper layer, called the subcloud layer, given its correspondence with the lifting condensation level calculated from environmental-mean air (black). For the mixed-layer and subcloud-layer top distributions, the thicker line is the mean of distributions calculated using individual height methods. (b) A schematic showing how vertical gradients in  $q$  and  $\theta$  compensate to weaken the vertical gradient in  $\theta_v$ . (c) 69 circle-mean profiles for  $q$ ,  $\theta$ , and  $\theta_v$ . The black line is the campaign-mean across all profiles, and colored profiles correspond to time (dark to lighter blue over time). Dotted lines mark the mixed-layer height and subcloud-layer height. The difference between the subcloud-layer top and mixed-layer top heights indicates the transition layer. (d) Two individual dropsonde profiles: one at 1606 UTC 31 Jan 2020 exhibiting a rare “jump-like” structure (black) and another at 1618 UTC 31 Jan 2020 exhibiting a more typical structure with smoother vertical gradient at the subcloud-layer top (gray).

sensors, such as in EUREC<sup>4</sup>A’s RD41 dropsondes, have rapid time constants and do not require time-lag corrections at the warmer temperatures in the lowest kilometers of the atmosphere. A comparison of dropsonde moisture profiles with higher-frequency (1 Hz) moisture measurements from the ATR-42 (not shown) further supports this inference that smooth vertical gradients are not an artifact of slow sensor response times.

The presence of a finite-thickness transition layer introduces ambiguity in the application of the mixed-layer theory, whose entrainment closures are based upon a canonical jump-like structure at the subcloud-layer top. We address this uncertainty through the introduction of effective parameters estimated through a Bayesian approach, as described in section 4c.

*b. Evidence that vertical thermodynamic gradients are small*

Another key assumption in mixed-layer theory is that subcloud-layer thermodynamic variables can be represented

by a single vertically well-mixed value. To test this assumption, we compare the magnitude of vertical gradients relative to variability about vertically averaged mean values across soundings. We do this in two steps. We first calculate the root-mean-square error (RMSE) from assuming a vertical, perfectly well-mixed profile relative to the observed profile up to the mixed-layer top. Second, this RMSE is compared with the standard deviation  $\sigma$  calculated for all mixed-layer mean values over the campaign (from circle-mean data), as the fractional difference  $[(\sigma - \text{RMSE})/\sigma] \times 100$ . A perfectly well-mixed layer would have values of 100%, and values near 100% indicate that the vertical variability about the mean for a particular sonde is much smaller than the variability among sondes. For  $q$ , the fractional difference is  $83\% \pm 3.2\%$  across circle-mean data, with the values denoting the mean and standard deviation. Similarly, the fractional difference for potential temperature is  $76\% \pm 6.0\%$ , with the smaller value for potential temperature resulting from its smaller variability about the mean value.

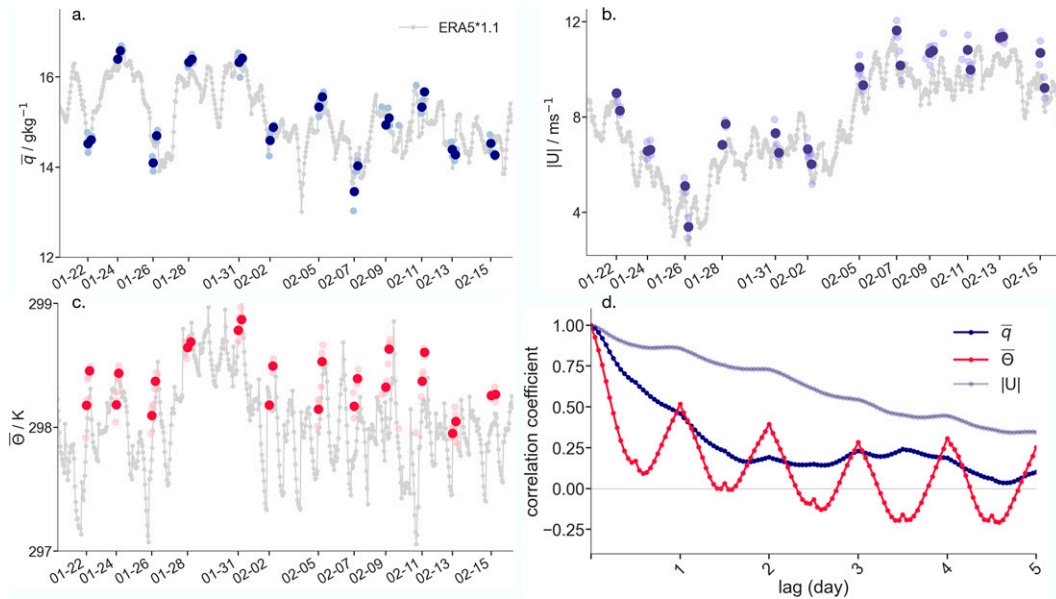


FIG. 3. Evolution of (a) subcloud-layer mean specific humidity  $\bar{q}$ , (b) 10 m wind speed, and (c) subcloud-layer mean potential temperature  $\bar{\theta}$  for circle-mean data (lighter circle) and circling-mean data (darker circle), compared with hourly ERA5 data (light gray). Note that ERA5 moisture displays a dry bias (Bock et al. 2021), and here ERA5 specific humidity is multiplied by a factor of 1.1. (d) The auto-correlation coefficients at various time lags calculated from hourly ERA5 data for  $\bar{q}$  and  $\bar{\theta}$ , interpolated to the same heights as the in situ data, and the 10 m wind speed.

[In appendix B, Fig. B1 also illustrates that what we call the mixed layer is indeed well-mixed vertically—with notable exceptions on 24 January (Figs. B1c,d), and 7 February 2020 (Figs. B1o,p), identified as having many cold pools (Touze-Peiffer et al. 2022), which are expected to cause deviations away from a well-mixed profile.] On this basis, we infer that vertical gradients are small and provide initial justification for their omission from the mixed-layer description. A posteriori support for this conclusion is provided by additional analysis in section 5.

Beyond the magnitude of vertical gradients, another question is the extent to which variability in vertical gradients encodes differences in variability among subcloud layers. We find that rank correlations (Kendall and Spearman) and Pearson correlations of  $\partial\theta/\partial z$  and  $\partial q/\partial z$  with  $h$ ,  $\bar{\theta}$ , and  $\bar{q}$  are below 0.3, suggesting that the strength of vertical gradients does not strongly differentiate subcloud layers.

### c. Moisture variability is the primary mode of subcloud-layer thermodynamic variability

We find that the subcloud layer varies thermodynamically primarily through variability in  $\bar{q}$ , and this moisture variability controls nearly all variability in subcloud-layer moist static energy (MSE), with a correlation coefficient  $r = 0.99$  between  $\bar{q}$  and mean subcloud-layer MSE. MSE is defined as  $c_p T + \ell_v q + gz$  where  $c_p$  is the specific heat at constant pressure,  $T$  is the absolute pressure in Kelvin,  $\ell_v$  is the specific enthalpy of vaporization,  $q$  is the water vapor specific humidity,  $g$  is the gravitational constant, and  $z$  is height above the surface. The height of the subcloud layer is defined using the  $\theta_v$ -gradient method, and subcloud-layer means,  $\bar{q}$  and  $\bar{\theta}$ , are defined as the density-weighted means from 50 m to this height.

One way to compare variability in  $\bar{q}$  and  $\bar{\theta}$  is by diagnosing their contribution to variability in vertical length scales. In the circle-mean aggregated data, anomalies in  $\bar{q}$  relative to the campaign-mean have a Pearson correlation coefficient  $r = -0.71$  with  $h$  anomalies and  $r = -0.97$  with anomalies in the LCL, showing that variability in different vertical heights is strongly associated with  $\bar{q}$  variability. Anomalies in  $\bar{\theta}$ , by contrast, have a Pearson correlation coefficient of only  $-0.5$  with anomalies in the LCL and  $-0.24$  with  $h$  anomalies. Warmer temperatures are also associated with increased humidity, which would lower the LCL, so the weak anticorrelation with potential temperature variability could reflect the compensating effects of temperature and humidity on the LCL.

Continuous ERA5 data, which are found to vary coherently with observations despite a dry bias in moisture [see Fig. 3a and Bock et al. (2021)], allow for estimating other modes of thermodynamic variability. ERA5 assimilated EUREC<sup>4</sup>A dropsonde and radiosondes, although ongoing analysis of winds shows that the assimilation of local soundings did not strongly influence the reanalysis (G. George 2022, personal communication). From these continuous ERA5 data, we find the  $\bar{q}$  signal, averaged for the same about 220 km-diameter circular domain as the observations (Fig. 1), de-correlates after approximately 2 days, with an auto-correlation coefficient that decreases from 0.98 after 1 h to 0.19 after 48 h (Fig. 3d). That moisture is mostly de-correlated after 2 days aligns well with the mean gap of 2 days between EUREC<sup>4</sup>A flights, indicating that the research flights sample independent realizations of synoptic moisture variability. The 10 m wind speed is highly auto-correlated, with an auto-correlation coefficient of 0.74 after 2 days and 0.48 after 8 days (Fig. 3d). The wind speed signal de-correlates after

10 days with  $r = 0.04$ , demonstrating the dominance of lower-frequency surface wind speed variability.

Another way of analyzing thermodynamic variability is performing fast Fourier transformations. The fast Fourier transformation of  $\bar{\theta}$  has a strong peak in the power spectral density at a 24 h frequency, whereas a diurnal signal is not seen in  $\bar{q}$  (not shown). Variability in  $\bar{\theta}$  is smaller in magnitude (Fig. 3c) and appears to be largely diurnal, potentially driven by variability in shortwave radiative heating (Albright et al. 2021).

#### 4. Mixed-layer theory for subcloud-layer moisture and heat

We first introduce the mixed-layer theory framework (section 4a). An important assumption in this theory is that the subcloud layer is well-mixed, which was shown to be the case, at least below the transition-layer base (section 4b). The existence of a finite-depth transition layer and its vertical gradients, however, introduces challenges into the application of mixed-layer theory, particularly its assumption that the interface between the subcloud layer and cloud layer is vanishingly thin (e.g., Lilly 1968; Stevens 2006). EUREC<sup>4</sup>A observations allow us to test the adequacy of this interpretive framework despite the presence of the finite-thickness transition layer.

##### a. Theory and closure assumptions

For a subcloud-layer scalar  $\vartheta$  after performing a Reynolds decomposition on the conservation equation ( $D\vartheta/Dt = Q_\vartheta$ , where  $Q_\vartheta$  is a diabatic source term) and integrating over the depth of the layer, the mixed-layer budget of  $\vartheta$  can be written as

$$hS_\vartheta = \overline{w'\vartheta'}|_0 - \overline{w'\vartheta'}|_1. \tag{1}$$

We neglect the horizontal gradients in  $\overline{w'\vartheta'}$ , which are small compared to the vertical gradients.  $S_\varphi$  includes the contribution of the mean flow to the material derivative, as well as the diabatic source term,  $Q_\varphi$ . This diabatic source term  $Q_\varphi$  can include radiation or precipitation and evaporation effects, but we set  $Q_\vartheta = 0$  for moisture, neglecting the influence of evaporating precipitation on the subcloud-layer moisture budget, but we do account for radiation in the heat budget ( $Q_\theta \neq 0$ ). The equation expresses that the vertical divergence of the turbulent flux balances the sum of the nonturbulent processes, denoted by  $S_\vartheta$  (e.g., Betts 1976; Stevens 2006). The thickness of the layer is  $h$ . The subscript 0 denotes values at the lower interface of the bulk layer (ocean-to-subcloud-layer interface), and the subscript 1 denotes values at the upper interface (the subcloud-to-cloud layer interface), and  $w$  refers to the vertical velocity.

The flux at an interface  $i$  is given as the product of the velocity relative to the mean flow and a “jump”:

$$\overline{w'\vartheta'}|_i = -V_i\Delta_i\vartheta, \tag{2}$$

where  $\Delta_i\vartheta$  defines the change in  $\vartheta$  across the interface, from top to bottom, so that  $\Delta_1\vartheta = \vartheta_1 - \bar{\vartheta}$  and  $\Delta_0\vartheta = \bar{\vartheta} - \vartheta_0$ .

With this notation, we can rewrite Eq. (1) as

$$hS_\vartheta = -V_0\Delta_0\vartheta + V_1\Delta_1\vartheta. \tag{3}$$

The first term on the right-hand side  $V_0\Delta_0\vartheta$  defines a surface flux wherein the surface exchange velocity  $V_0$  denotes the product of the 10 m horizontal wind speed,  $\|U\|$  (wherein easterly is defined as negative), and a dimensionless parameter  $C_d$  following surface-layer similarity theory (e.g., Stevens 2006). Note that  $-V_0\Delta_0\vartheta$  is positive when surface values are larger than subcloud-layer values, which is almost always the case for potential temperature and specific humidity. The dimensionless parameter  $C_d$  depends on the surface roughness, the structure of the surface layer, and the stability of this layer but is generally taken to be constant and equal to 0.0011 (e.g., Deardorff 1972; Fairall et al. 2003). In this analysis, we set  $C_d = 0.0010$ . Our smaller value compensates for the larger difference between the surface and subcloud-layer values, compared to the typical difference taken between the surface and 20 m value (e.g., Fairall et al. 2003).

##### 1) ENTRAINMENT CLOSURE

In Eq. (3)  $V_1$  represents the diabatic growth of the subcloud layer into the overlying fluid and is taken to equal the entrainment rate  $E$  (e.g., Stevens 2006). The fundamental processes controlling entrainment remain poorly understood and represented (e.g., Fedorovich et al. 2004; Canut et al. 2012). The most basic approach, proposed by Lilly (1968), is to represent the turbulent entrainment flux at the subcloud-layer top as a fixed fraction of the surface turbulent flux:

$$E = -\frac{AV_0\Delta_0\theta_v}{\Delta_1\theta_v}. \tag{4}$$

This closure is known as the “zero-order jump model” for  $E$ , as the jump occurs over a transition layer of zero thickness. A zero-order jump model is made in analogy with the sharp discontinuity seen in stratocumulus mixed layers (e.g., Lilly 1968; Deardorff 1972) and dry convective boundary layers (e.g., Tennekes 1973; Stull 1976).

The constant  $A$  defines the entrainment “efficiency” and varies between 0 and 1. The end member of  $A = 0$  refers to total frictional dissipation of the surface buoyancy flux and no entrainment at the layer-top, whereas  $A = 1$  refers to zero frictional dissipation, and the entire surface buoyancy flux being available for entrainment (Lilly 1968). The jump,  $\Delta_1\theta_v$ , is positive and models the resistance that entrainment feels when tasked with mixing a relatively more buoyant fluid into the turbulent layer.

As discussed in section 4a, the subcloud layer is not, except in rare cases, characterized by such a zero-order jump structure and instead exhibits vertical gradients over a finite depth. Such vertical gradients over a finite thickness are consistent with finite-thickness entrainment zones seen in large-eddy simulations, in what is often called a first-order jump model (e.g., van Zanten et al. 1999; Canut et al. 2012). The zero- and first-order jump models are contrasted schematically in Fig. 4.

We attempt to accommodate the ambiguity from the transition layer by introducing coefficients  $C_q$  and  $C_\theta$ , which scale jumps at the top of the layer and compensate for possible errors in our choice of the subcloud-layer height  $h$  and uncertainty in the depth over which the jumps are computed. The scaling coefficient approach is similar to the linear mixing-line



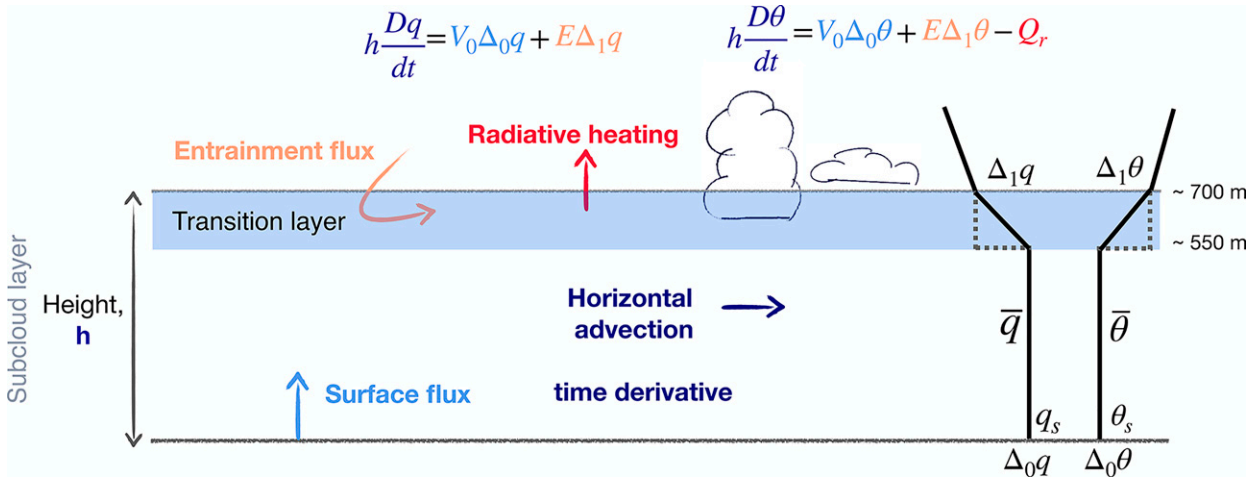


FIG. 4. Schematic of subcloud-layer budgets, as described in Eqs. (8) and (9). Descriptions of the surface fluxes ( $V_0\Delta_0\theta$ ), entrainment fluxes ( $E\Delta_1\theta$ ), material derivatives ( $D\theta/dt$ ), and clear-sky radiative heating term ( $Q_r$ ) are given in sections 4b and 4c. The height  $h$  refers to the depth of the subcloud layer, which includes both a well-mixed layer and a transition layer. Also shown are idealized profiles of specific humidity  $q$  and potential temperature  $\theta$  in keeping with the zero-order jump model (dotted lines) and the first-order model, similar to what is done in this study (solid lines).

model that represents cloud-layer air mixing into the mixed layer (Betts and Ridgway 1989). Whereas our formulation is similar to the “transfer coefficient” approach in Neggers et al. (2006) and Zheng (2019), these studies take differences between values in the free troposphere and the subcloud layer, whereas we consider values across the transition layer. The jumps  $\Delta_1q$ ,  $\Delta_1\theta$ , and  $\Delta_1\theta_v$  are formulated as

$$\Delta_1q = C_q(q_{h+} - \bar{q}_{h-}), \quad (5)$$

$$\Delta_1\theta = C_\theta(\theta_{h+} - \bar{\theta}_{h-}), \quad (6)$$

$$\Delta_1\theta_v = \Delta_1\theta + 0.61(\bar{\theta}\Delta_1q + \bar{q}\Delta_1\theta). \quad (7)$$

The subscript  $h+$  refers to the value of  $q$  or  $\theta$  above  $h$ , computed as the average from  $h$  to  $h + 100$  m.  $\bar{q}_{h-}$  or  $\bar{\theta}_{h-}$  are averages from 50 m to the mixed-layer top defined from the linearized relative humidity method (see appendix A), though it is insensitive to defining the mixed-layer top using other methods. The choice of averaging up to the mixed-layer top, rather than up to  $h$ , to calculate these jumps is motivated by the desire to exclude transition-layer air in the average. Due to sub-circling variability in  $h$ , excluding transition-layer air can best be achieved by a conservative (and therefore lower-altitude) choice of averaging height. The choice of averaging from  $h + 100$  m is to reduce small-scale variability associated with values at a single altitude. The ultimate magnitude of the entrainment fluxes or residuals in the budgets are not affected by selecting values at  $h$ , or averaging up to 50, 100, or 150 m above  $h$ , though it does influence the relative magnitudes of the entrainment rate,  $E$ , compared to the jumps. Ultimately the budget analysis depends on the product of  $E$  times the jump, and so defining the jump over a larger layer increases the jump and decreases  $E$ .

## 2) BUDGET EQUATIONS FOR SUBCLOUD-LAYER MOISTURE AND HEAT BALANCES

Combining these assumptions, the budget for Eq. (1) for specific humidity  $\bar{q}$  is

$$h \left[ \frac{\partial \bar{q}}{\partial t} + (\mathbf{u} \cdot \nabla \bar{q}) \right] = -C_{d\parallel} U \|\Delta_0 q - \frac{A_e V_0 \Delta_0 \theta_v}{\Delta_1 \theta_v} \Delta_1 q. \quad (8)$$

The  $\bar{q}$  balance is between a surface latent heat flux,  $-C_{d\parallel} U \|\Delta_0 q$ , which moistens the layer from a saturated ocean surface moisture source,  $q_s$ , wherein  $\Delta_0 q = \bar{q} - q_s < 0$ ; an entrainment flux,  $-[(A_e V_0 \Delta_0 \theta_v)/(\Delta_1 \theta_v)] \Delta_1 q$ , which imports drier cloud-layer air into the subcloud layer, wherein  $E$  is defined in Eq. (4) and  $\Delta_1 q < 0$ ; and large-scale horizontal advection,  $\mathbf{u} \cdot \nabla \bar{q}$  and a time derivative,  $\partial \bar{q}/\partial t$ , both of which can either moisten or dry the subcloud layer. We neglect phase changes, such as associated with evaporating precipitation within the subcloud layer.

For subcloud-layer mean potential temperature  $\bar{\theta}$ , the budget equation is

$$h \left[ \frac{\partial \bar{\theta}}{\partial t} + (\mathbf{u} \cdot \nabla \bar{\theta}) \right] = -C_{d\parallel} U \|\Delta_0 \theta - \frac{A_e V_0 \Delta_0 \theta_v}{\Delta_1 \theta_v} \Delta_1 \theta + h Q_r. \quad (9)$$

Equation (9) includes a surface sensible heat flux,  $-C_{d\parallel} U \|\Delta_0 \theta$ , which warms the subcloud layer given  $\Delta_0 \theta = \bar{\theta} - \theta_s < 0$ ; an entrainment flux  $[-(A_e V_0 \Delta_0 \theta_v)/(\Delta_1 \theta_v)] \Delta_1 \theta$ , which brings warmer cloud-layer air into the subcloud layer; large-scale horizontal advection  $\mathbf{u} \cdot \nabla \bar{\theta}$ , which could either warm or cool the layer; a time-derivative  $\partial \bar{\theta}/\partial t$ , which is predominantly associated with the diurnal cycle; and a clear-sky radiative heating term  $Q_r$ , another cooling term. We again neglect phase changes, such as evaporating precipitation. This heat balance is more difficult to

constrain, both because it involves more terms and because the magnitude of individual terms is smaller. Also note that these kinematic fluxes can be converted to dynamic fluxes by multiplying by the air density  $\rho$  and  $\ell_v$  for specific humidity, and air density and  $c_p$  for potential temperature.

The processes in the  $\bar{q}$  budget [Eq. (8)] and  $\bar{\theta}$  budget [Eq. (9)] are illustrated schematically in Fig. 4.

*b. Observational estimates of terms in mixed-layer theory budgets*

Here we describe how the different terms in Eq. (8) and Eq. (9) are calculated from observations, except for entrainment, which is the focus of section 4c. Clear-sky, aerosol-free radiative heating profiles for EUREC<sup>4</sup>A dropsondes and radiosonde profiles are calculated in Albright et al. (2021). Large-scale horizontal moisture advection,  $\mathbf{u} \cdot \nabla \bar{q}$ , and potential temperature advection,  $\mathbf{u} \cdot \nabla \bar{\theta}$ , are calculated in George et al. (2021) using the regression method from Bony and Stevens (2019). We estimate the time derivatives or storage terms,  $\partial \bar{q} / \partial t$  and  $\partial \bar{\theta} / \partial t$ , as the ordinary least squares regression slope of the three circle-means per circling-mean. Estimating this derivative as the regression slope for the approximately 30–36 individual soundings per circling yields similar results ( $r = 0.82$ ), yet these soundings are more affected by small-scale variability than are circle-means. For uncertainty estimates, we calculate the standard error of the three circle-mean data per circling-mean for all terms in Eqs. (8) and (9), except for uncertainty on the time derivative, which we take to be the standard error on the regression slope.

**SURFACE FLUXES**

Bulk estimates of surface fluxes are calculated as  $-C_d \|U\| \Delta_{0\theta}$  [Eq. (14) and Eq. (15)]. The difference  $\Delta_{0\theta}$  is taken between the mixed-layer mean and surface value and is negative, yielding positive surface fluxes. Estimates are  $6.3 \pm 2.7 \text{ W m}^{-2}$  for the sensible heat flux and  $166 \pm 54 \text{ W m}^{-2}$  for the latent heat flux, with the notation denoting the mean and standard deviation. For the sensible heat fluxes, we subtract 0.25 K from R/V *Meteor* sea temperatures measured at few-meter depth to account for the “cool skin” effect that sea surface temperatures at the surface are cooler than at few-meter depth (e.g., Fairall et al. 2003). The bulk estimates of surface sensible and latent heat fluxes agree well, both in terms of magnitude and variability, with three alternative, but collocated estimates of these fluxes: bulk estimates from the R/V *Meteor*, fluxes calculated with the COARE algorithm (Fairall et al. 2003) using HALO dropsonde data, and ERA5 surface fluxes (Table 2). Pearson correlation coefficients of our bulk sensible heat flux estimates are  $r = 0.81, 0.82,$  and  $0.72$  with these three estimates, respectively. For the latent heat fluxes, the correlations are  $r = 0.84, 0.92,$  and  $0.95,$  respectively. These flux values are consistent with climatological values, for instance as shown by Yu et al. (2004) and Bigorre and Plueddemann (2021) (about  $160\text{--}170 \text{ W m}^{-2}$  for the latent heat flux and  $6\text{--}8 \text{ W m}^{-2}$  for the sensible heat flux) with differences being consistent with sampling errors associated with the observations being made for slightly different locations or time periods.

TABLE 2. Campaign-mean and standard deviation of different terms as calculated from the 24 circling-mean data (about 3-hourly time scale) averaged along the “EUREC<sup>4</sup>A circle” for surface latent and sensible heat fluxes, entrainment fluxes, horizontal advection terms, and net radiative heating. Values of  $A_e$  are from the Bayesian inversion, and the effective jumps are calculated by from Eqs. (5) and (6) using the mean values of  $C_q$  and  $C_\theta$ . For the surface flux terms, “bulk” refers to bulk theory formulations, “Meteor” refers to measurements from the R/V *Meteor* instead of dropsondes, and “COARE” refers to the COARE algorithm. Horizontal advection and net radiative heating are values averaged over the subcloud-layer depth.

|   | Units                               | Mean                  | St dev.               |
|---|-------------------------------------|-----------------------|-----------------------|
| $F_q$ bulk, dropsondes  | $\text{W m}^{-2}$                   | 166                   | 56                    |
| $F_q$ bulk, Meteor  | $\text{W m}^{-2}$                   | 165                   | 48                    |
| $F_q$ COARE, dropsondes   | $\text{W m}^{-2}$                   | 162                   | 45                    |
| $F_q$ ERA5  | $\text{W m}^{-2}$                   | 178                   | 49                    |
| $F_\theta$ bulk, dropsondes                                     | $\text{W m}^{-2}$                   | 6.3                   | 2.7                   |
| $F_\theta$ bulk, Meteor   | $\text{W m}^{-2}$                   | 6.5                   | 3.8                   |
| $F_\theta$ COARE, dropsondes                                    | $\text{W m}^{-2}$                   | 6.0                   | 6.1                   |
| $F_\theta$ ERA5   | $\text{W m}^{-2}$                   | 10                    | 4.5                   |
| $E$   | $\text{mm s}^{-1}$                  | 20.4                  | 7.9                   |
| $A_e$   | —                                   | 0.43                  | 0.056                 |
| $C_q$   | —                                   | 1.26                  | 0.34                  |
| $C_\theta$  | —                                   | 1.15                  | 0.31                  |
| $\Delta_1 q = C_q(q_{h+} - \bar{q}_{ h_-})$                     | $\text{g kg}^{-1}$                  | −2.32                 | 0.597                 |
| $\Delta_1 \theta = C_\theta(\theta_{h+} - \bar{\theta}_{ h_-})$ | K                                   | 0.782                 | 0.115                 |
| $\Delta \theta_v$   | K                                   | 0.359                 | 0.0297                |
| $E \Delta q$  | $\text{W m}^{-2}$                   | −128                  | 52.8                  |
| $E \Delta \theta$   | $\text{W m}^{-2}$                   | 18.0                  | 6.47                  |
| $\mathbf{u} \cdot \nabla \bar{q}$                               | $\text{g kg}^{-1} \text{ m s}^{-1}$ | $1.59 \times 10^{-5}$ | $2.12 \times 10^{-5}$ |
| $\mathbf{u} \cdot \nabla \bar{\theta}$                          | $\text{K m s}^{-1}$                 | $8.51 \times 10^{-3}$ | $8.46 \times 10^{-3}$ |
| $Q_{\text{rad,clr}}$  | $\text{K day}^{-1}$                 | −0.853                | 1.01                  |

The surface turbulent flux  $F_{\theta_v}$ , which is used to compute  $E$ , is defined as  $F_{\theta_v} = F_\theta + 0.608 \bar{\theta} F_q$ , wherein 0.608 is a thermodynamic constant that relates the molecular weight of water relative to that of dry air.  $F_{\theta_v}$  relates to surface buoyancy flux by a factor of  $g/\bar{\theta}$ , which then denotes the time rate of change of turbulent kinetic energy production.  $F_{\theta_v}$  fluxes estimated from mixed-layer theory or bulk methods are  $16 \pm 5.2 \text{ W m}^{-2}$ , which agree well with the three other surface flux estimates in magnitude and variability, with correlation coefficients around  $r = 0.9$ .

*c. Bayesian inversion of uncertain terms in entrainment fluxes*

The most uncertain terms in Eq. (8) and Eq. (9) relate to the entrainment fluxes: the effective entrainment efficiency ( $A_e$ ) and the scaling parameters for the jumps ( $C_q$  and  $C_\theta$ ). The entrainment exchange velocity  $E$  [Eq. (4)] and fluxes at the subcloud-layer top have long been challenging to measure observationally (e.g., Lenschow et al. 1999; Kawa and Pearson

1989; Stevens et al. 2003a) or estimate from simulations (e.g., Moeng et al. 1999; Bretherton et al. 1999; Vogel et al. 2020).

There are a lack of foregoing constraints on these jumps, and from the trade wind observations, there are ambiguities associated with how to define the jumps at the upper interface (Fig. 2c). Given these uncertainties, we constrain the parameters,  $\Theta = (A_e, C_q, C_\theta)$ , using a Bayesian framework. This approach allows for estimating a joint distribution of parameters  $\Theta$  that are most likely to explain the observed data. The values of  $C_q$ ,  $C_\theta$ , and  $A_e$  should be physical, and synoptic variability should be explained without having to vary these parameters.

The Bayesian approach is similar to other optimization techniques, yet it yields joint posterior distributions and thus provides an estimate of uncertainty for the constrained parameters. Following Bayes rules, we invert for the joint posterior distribution of  $\Theta$ :

$$P(\Theta|y_{\text{obs}}) \propto P(y_{\text{obs}}|\Theta)P(\Theta). \quad (10)$$

Sampled sets of parameter values,  $\Theta$ , are used with observed estimates of the other terms to model subcloud-layer moisture and temperature budgets,  $y_{\text{obs}}$ , following Eq. (8) and Eq. (9). We model the likelihood  $P(y_{\text{obs}}|\Theta)$  such that the residuals of the subcloud-layer moisture and heat budgets are normally distributed around zero with standard deviations  $\sigma_q$  and  $\sigma_\theta$ , respectively. The likelihood  $P(y_{\text{obs}}|\Theta)$  is thus formulated based on the multivariate Gaussian distribution of the modeled subcloud-layer moisture and temperature budgets:

$$P(y_{\text{obs}}|\Theta) \sim N[0, \Sigma^2(\Theta)]. \quad (11)$$

$$\Sigma^2(\Theta) = \begin{bmatrix} \sigma_q^2 & 0 \\ 0 & \sigma_\theta^2 \end{bmatrix}. \quad (12)$$

This likelihood expresses the probability of closing the moisture and heat budgets, or jointly obtaining residuals normally distributed around zero for both budgets given parameters  $\Theta$ . We set the off-diagonal terms to zero in Eq. (12), meaning that there is no covariance between residuals in the moisture and heat budget. We assume a standard deviation  $\sigma_q$  of  $1 \times 10^{-8} \text{ kg}^{-1} \text{ s}^{-1}$ , or  $17 \text{ W m}^{-2}$  when converted from a kinematic to dynamic flux. For potential temperature, the standard deviation  $\sigma_\theta$  is chosen to be  $3 \times 10^{-6} \text{ K s}^{-1}$  or  $2.5 \text{ W m}^{-2}$ , though our results are insensitive to these choices. The posterior distribution  $P(\Theta|y_{\text{obs}})$  then represents the distribution of parameter values that are most likely to close the budgets given observed variability.

For the prior distribution  $P(\Theta)$  on  $A_e$ , we choose a normal prior with mean of 0.2 and standard deviation 0.4,  $\mathcal{N}(0.2, 0.4^2)$ . A common view of  $A_e$  is the ratio of minimum to maximum buoyancy fluxes, when assuming that the minimum buoyancy flux occurs at the subcloud-layer top, and that the transition from the negative, minimum to zero buoyancy flux occurs over an infinitely thin layer. Its value is often taken to be 0.2 (Lilly 1968; Stull 1976; Tennekes and Driedonks 1981; Driedonks 1982; Pino et al. 2003), motivating our choice of normal prior with mean 0.2. Assuming that the source of entrainment is surface buoyancy fluxes (rather than other processes, such as radiative

cooling, or evaporative cooling by clouds as in Stevens (2007)), a value of  $A_e$  greater than one is energetically inconsistent with our assumptions. Obtaining a posterior distribution of  $A_e$  that does not exceed one serves as a physical test of the model. For the scaling parameters, we model the prior distributions for  $C_q$  and  $C_\theta$  as a normal distribution with mean 1 and standard deviation of 0.5.

Sampling is performed using the Metropolis–Hastings algorithm (Metropolis et al. 1953; Hastings 1970), and we run the model for 60 000 samples, four times (four “chains”), though results converge after 30 000 samples. The first 10 000 samples are discarded for each chain, yielding 200 000 samples. Results are consistent among chains, indicating that our model is adequately sampled.

## 1) BAYESIAN INVERSION RESULTS

Notably, the entrainment efficiency,  $A_e$ , is well constrained by the Bayesian inversion and has a maximum likelihood estimate (MLE) posterior value of 0.43 and a 5%–95% credible interval of 0.34–0.53 (Fig. 5). Its marginal posterior distribution is similar regardless of the prior distribution;  $A_e$  being larger than 0.2 is consistent with it being an effective parameter that reflects the existence of a finitely thick transition layer, as previously discussed. Using Sahelian convective boundary layer observations, Canut et al. (2012) also found evidence for an entrainment efficiency larger than 0.2 given a finite-thickness entrainment zone, though in their case wind shear over the entrainment zone contributed to a larger value. Wind shear over the transition layer is, however, small during EUREC<sup>4</sup>A (cf. Fig. B2). Whether or not this value of  $A_e$  is consistent with direct numerical simulation (Garcia and Mellado 2014) and large-eddy simulation (Fedorovich et al. 2004) of the convective boundary layer, which suggest values closer to 0.2, is unclear. A larger value of  $A_e$ , as in the case of van Zanten et al. (1999), may result from how we define the jumps and the depth of the layer, whose values are greater than those in idealized LES (as discussed by Fedorovich et al. (2004)).  $A_e > 0.2$  could also be indicative of cloud processes within the transition layer contributing to the mixing (cf. Stevens (2007)), an idea we are exploring further in a separate study.

The mean posterior value of  $C_q$  is 1.26 with a 5%–95% credible interval of 0.74–1.89. The mean posterior value of  $C_\theta$  is 1.15 with a 5%–95% credible interval of 0.65–1.66 (Fig. 5). We multiply the mean posterior values of the transfer coefficients by the time-varying values of  $\Delta q$  and  $\Delta \theta$  [calculated following Eq. (5) and Eq. (6)] to obtain specific humidity and potential temperature jumps used to calculate the entrainment flux. The strong covariance between  $C_q$  and  $C_\theta$ , with a Pearson correlation coefficient of  $r = 0.97$ , suggests that the same subcloud-layer eddies mix moisture and heat, consistent with physical expectation, and that knowing either  $C_q$  or  $C_\theta$  appears sufficient for scaling the jumps. That the parameters constrained by the Bayesian inversion are physical—namely, an  $0.2 < A_e \leq 1$  and scaling coefficients that strongly covary—acts as a first validation of mixed-layer theory.

Our entrainment rates are  $20.4 \pm 7.9 \text{ mm s}^{-1}$ , with values denoting the mean and standard deviation (Table 2). Similar to the surface fluxes, making a direct quantitative comparison with previous studies is difficult given that different regimes are sampled,

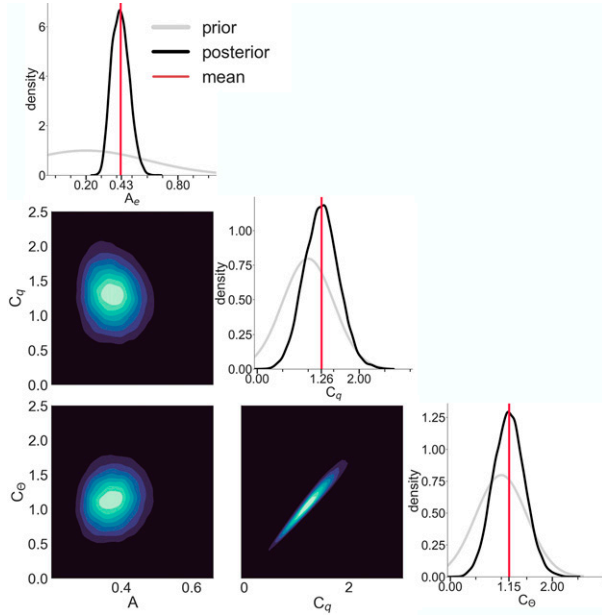


FIG. 5. Joint posterior distributions for the uncertain entrainment parameters  $A_e$ ,  $C_q$ , and  $C_\theta$ , with lighter colors referring to more frequently sampled parameter combinations. For the marginal posterior distributions (black), the marginal prior distribution (gray) and mean of the posterior distribution (red) are also shown.

such as a trade wind or stratocumulus boundary layer, as well as different vertical levels (e.g., cloud-top versus cloud-base). There are a number of foregoing estimates of cloud-top entrainment rates in stratocumulus regimes: during the DYCOMS-II field study southwest of California, Stevens et al. (2003b) find values  $3.9 \pm 1 \text{ mm s}^{-1}$ ; also using in situ data but in the southeast Pacific, Caldwell et al. (2005) estimate rates of  $4 \pm 1 \text{ mm s}^{-1}$ ; using satellite measurements for a transect from  $35^\circ$  to  $15^\circ\text{N}$ , Kalmus et al. (2014) estimate  $3.5 \pm 1.5 \text{ mm s}^{-1}$ ; and using in situ observations from the MAGIC field campaign between California and Hawaii, Ghate et al. (2019) estimated cloud-top entrainment rates of  $7.83 \pm 5.23 \text{ mm s}^{-1}$  in closed cellular stratocumulus cloud conditions. The larger entrainment rates during EUREC<sup>4</sup>A are plausible considering the much weaker stability of the capping layer compared to stratocumulus regimes. In the Sahelian boundary layer, Canut et al. (2012) estimate a large range of cloud-top entrainment rates from about  $10\text{--}150 \text{ mm s}^{-1}$  (their Figs. 10, 11). In large-eddy simulations of trade wind regions, Vogel et al. (2020) find a mean entrainment rates of  $14 \text{ mm s}^{-1}$ , with lower values compared to observed EUREC<sup>4</sup>A values likely due to the coarser vertical resolution leading to a larger  $\Delta\theta_v$ -jump.

## 2) JUSTIFICATION FOR LARGER ENTRAINMENT EFFICIENCY $A_E$ FROM THEORY

Before presenting the resulting budgets, we present two expository examples that contextualize the larger effective entrainment parameter  $A_e$  from the Bayesian inversion that accounts for a finitely thick transition layer.

First, performing a Reynolds decomposition on the conservation equation,  $D\theta/Dt = Q_\theta$ , and integrating over a layer above

and below  $h$  from  $h_+ = h + \epsilon$  to  $h_- = h - \epsilon$  for some small  $\epsilon$  yields an expression for  $E$ , wherein  $\theta_{v+}$  is the value at  $h_+$ , and  $\delta h = 2\epsilon$ :

$$E = \frac{-AV_0\Delta_0\theta_v}{\Delta_1\theta_v} + \frac{\delta h}{2\Delta_1\theta_v} \left( \frac{d\bar{\theta}_v}{dt} + \frac{d\theta_{v+}}{dt} \right). \quad (13)$$

The derivation for Eq. (13) is given in appendix C. Setting Eq. (4) and Eq. (13) equal for  $E$ , we consider that the second term on the right-hand side of Eq. (13) is absorbed to increase  $A$  in Eq. (4), which renders  $A$  as an effective parameter  $A_e$  that accounts for jumps occurring over a finite-thickness layer. This second term is what Garcia and Mellado (2014) called the ‘‘distortion and shape term,’’ although in their study of a clear-sky convective boundary layer, it was only a small (10%) contribution to a value of  $A \approx 0.2$ , associated with turbulent mixing.

A second justification is obtained by specifying that  $A_e$  is the value yielding the correct vertical flux divergence:

- 1) Modeling the subcloud layer with an infinitely thin transition layer (zero-order flux-jump model), the rate of warming or drying in the subcloud layer is given by the vertical flux gradient,  $\partial F/\partial z$ . The vertical flux divergence equals  $[F_0(1 + A)]/h$  if  $F_h = -AF_0$ , where subscripts 0 and  $h$  refer to the surface and subcloud-layer top, respectively, and  $F$  denotes the fluxes.
- 2) In the case of a finite-thickness transition layer, the flux minimum is not at the top of the subcloud layer, but rather at some height below  $h - \delta h$  (first-order flux-jump model; see, for instance, Fig. 1 in Fedorovich et al. (2004) for an illustration). In this case,  $A$  is still defined as the ratio of the minimum to maximum flux, and the vertical flux divergence over the layer of depth  $h - \delta h$  is  $[F_0(1 + A)]/(h - \delta h)$ .
- 3) Setting these two vertical flux divergences equal and replacing  $A$  in step (1) with  $A_e$  to introduce an effective parameter into the zero-order flux-jump model is  $[F_0(1 + A_e)]/h = [F_0(1 + A)]/(h - \delta h)$ , yielding  $A_e = [(1 + A)h]/(h - \delta h) - 1$ . For example, if  $A = 0.2$  as often assumed, and  $h = 710 \text{ m}$ , then  $A_e = 0.40$  for  $\delta h = 100 \text{ m}$ ,  $A_e = 0.52$  for  $\delta h = 150 \text{ m}$ , and  $A_e = 0.67$  for  $\delta h = 200 \text{ m}$ .

Fedorovich et al. (2004) argue that this apparent increase in  $A$  would arise, for instance if the depth of the subcloud layer is chosen to be above the height of the buoyancy flux minimum, which was not measured during EUREC<sup>4</sup>A.

## 5. Resulting moisture and temperature budgets

Adopting the mean parameter estimates from the Bayesian inversion, Fig. 6 shows that the bulk theory budgets close to within  $3.6 \text{ W m}^{-2}$  for moisture and  $2.9 \text{ W m}^{-2}$  for potential temperature for the campaign-mean and can largely explain synoptic variability.

For the moisture budget, the campaign-mean residual is 2.2% of the largest term, the surface latent heat flux. For synoptic variability, the residuals can have larger magnitude, yet uncertainty propagated from the individual terms crosses zero for 20 out of 24 circling-means, suggesting that residuals are unbiased and indistinguishable from zero to within uncertainty. The budgets also close equally well for daytime or nighttime (Fig. 6a). In



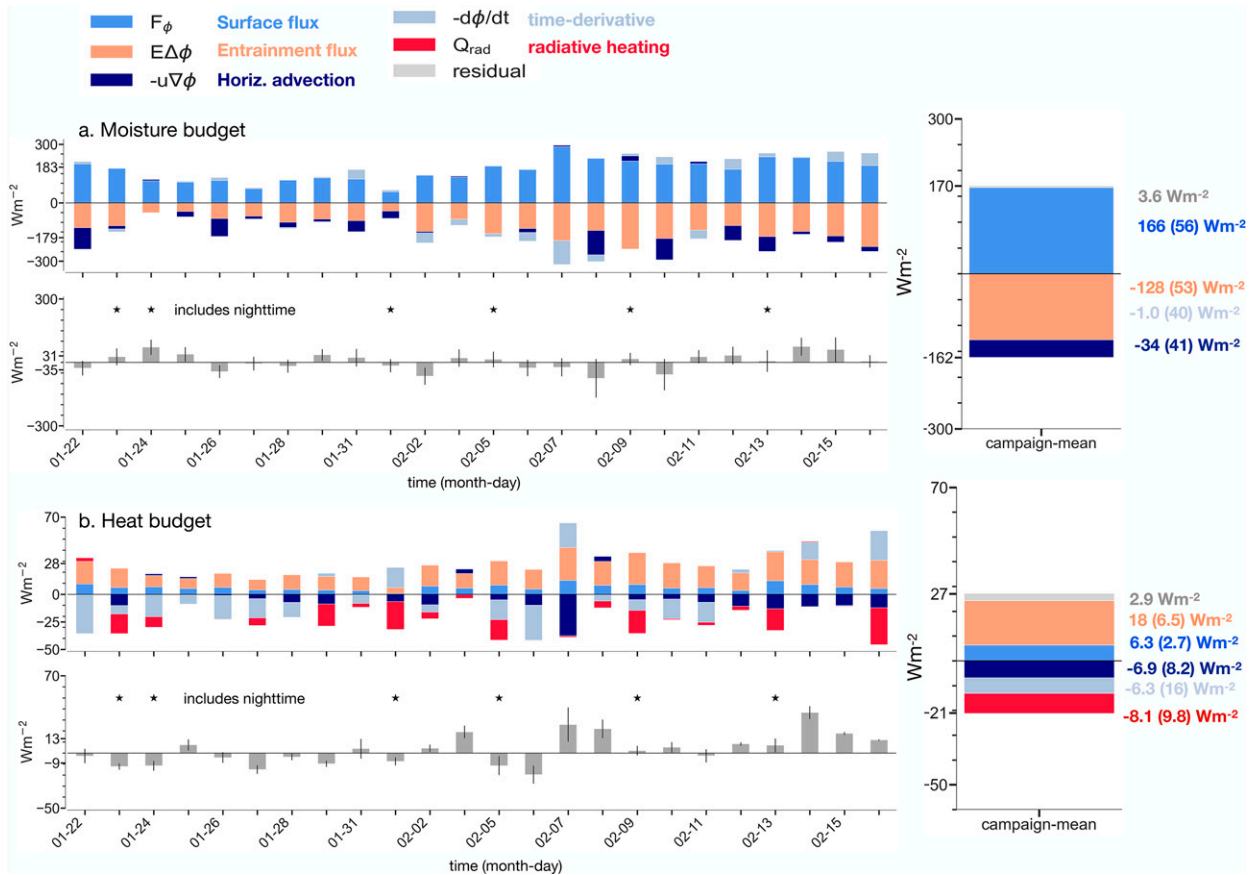


FIG. 6. Synoptic variation over time and campaign-mean moisture and heat balances, showing the surface flux (blue), entrainment flux (orange), large-scale horizontal advection (dark blue), the time derivative (light blue), clear-sky radiative cooling (red), and the residual term (gray). Note that time is not linear on this axis and refers to the different measurement periods. Black stars flag circling-means that include sondes launched during the nighttime. (a) The moisture balance and (b) the heat budget balance. The black error bar represents uncertainties in quadrature, added together for all terms: the 5%–95% Bayesian credible interval on entrainment parameters, and for the other terms, one standard deviation calculated across the three circling-means making up one circling-mean. In the residual panels, the intermediate y-axis ticks (around 30 and 10  $\text{W m}^{-2}$ ) denote the mean values of positive and negative residuals. (right) For the campaign-mean balance, values given correspond to the mean and standard deviation of each time across the campaign.

the heat balance, 14 out of 24 residuals are unbiased, with their uncertainty estimates crossing uncertainty, and as for moisture, the heat budget holds equally well for day and night (Fig. 6b).

Regarding the relative magnitude of physical processes, for the moisture budget, the dominant balance is between surface latent heat flux ( $166 \pm 56 \text{ W m}^{-2}$ ) and entrainment drying flux ( $-128 \pm 53 \text{ W m}^{-2}$ ), with a secondary role for large-scale moisture advection multiplied by  $h$  ( $-34 \pm 41 \text{ W m}^{-2}$ ) and the storage term multiplied by  $h$  ( $-1.0 \pm 40 \text{ W m}^{-2}$ ). The mean ratio between the surface latent heat flux and the entrainment drying flux is 1.39. The advection terms are the product of negative (easterly) winds and a negative difference from taking the difference of a colder, drier value in the east minus a warmer, moister value farther west. The net effect of this advection term on the balances is negative because it is subtracted from the left-hand side in Eq. (8) and Eq. (9).

In the heat budget, the entrainment flux ( $18 \pm 6.5 \text{ W m}^{-2}$ ) has roughly twice the magnitude of the other terms, which

have a similar magnitude of 6–8  $\text{W m}^{-2}$  (Fig. 6b). That the entrainment warming flux has a larger magnitude than the surface sensible heat flux is because the surface latent heat flux contributes strongly to the buoyancy fluxes, i.e., though the  $F_q$  contribution to  $F_{\theta_s}$ . Compared to the moisture budget, wherein surface fluxes balance entrainment fluxes to first-order, there is greater variability in the magnitude of individual terms in the heat budget. In certain cases (e.g., second circling-mean on 31 January 2020), the time-derivative term is larger than the entrainment flux. In the heat balance, radiative cooling of the layer, and the time-derivative and horizontal advection when they are cooling terms, are disproportionately balanced by entrainment warming. In three cases, the magnitude of the heat budget residuals are larger than the largest-magnitude term (second circling-mean on 2 February 2020, second circling-mean on 7 February 2020, second circling-mean on 13 February 2020). Note that setting  $h$  to be the mixed-layer top, rather than the subcloud-layer top results in slightly larger

residuals,  $6.9 \text{ W m}^{-2}$  for the heat budget and  $9.6 \text{ W m}^{-2}$  for the moisture budget.

One might be tempted to think that the flexibility afforded by the Bayesian framework allows for closing the budgets by construction.  $A_e$ ,  $C_q$ , and  $C_\theta$  are assumed to be constant, yet vertical profiles of moisture and potential temperature change across days, such that there is no guarantee that a fixed combination of  $A_e$ ,  $C_q$ , and  $C_\theta$  allows for budgets to close. We close moisture and heat budgets jointly, which provides a stronger constraint than closing a single budget. That is, in the moisture budget, drying by entrainment balances moistening by surface fluxes, whereas in the heat budget, both entrainment and surface fluxes warm the layer, such that each budget place counteracting constraints on the entrainment rate.

That the budgets close to within small residuals for most cases and the campaign-mean suggests that knowledge of the mean state in Eqs. (8) and (9) is sufficient to close the budgets, without knowledge of the vertical thermodynamic gradients or incorporating additional processes. The ratios of  $\partial\theta/\partial z$  and  $\partial q/\partial z$  multiplied by  $h/2$  to the jumps at the upper interface are small, with a mean value of 20% for  $q$  and 22% for  $\theta$ , providing further evidence that the influence of vertical gradients on the subcloud-layer budgets is small. The correlation of residuals with vertical gradients, moreover, informs whether the omission of vertical gradients from the budgets is justified. Indeed, correlations of residuals with vertical gradients are small: the correlations of  $\bar{\theta}$  residuals with  $\partial\theta/\partial z$  and  $\partial q/\partial z$  are 0.21 and  $-0.17$ , respectively, and the correlations of the  $\bar{q}$  residuals with  $\partial\theta/\partial z$  and  $\partial q/\partial z$  are 0.33 and  $-0.25$ , respectively.

*Is the remaining structure in residuals informative of missing processes?*

Structure in the residuals is indicative of observational error, structural issues in our formulations, or missing processes. The entrainment efficiency ( $A_e$ ) and the scaling coefficients on the jumps ( $C_q$  and  $C_\theta$ ) could, in principle, vary on a case-by-case basis with the thickness of the transition layer [cf. Eq. (13)], which we do not account for in the present analysis by assuming these parameters are constants. That said, the thickness of the transition layer does not strongly correlate with residuals in the moisture ( $r = 0.38$ ) or heat budgets ( $r = 0.20$ ). Regarding missing processes, we use two proxies for precipitation or precipitation-driven downdrafts, whose influences we neglect: cloud top height estimated from the WALES instrument onboard HALO (Konow et al. 2021), mindful that deeper clouds are more likely to precipitate (e.g., Stevens et al. 2016), and a cold pool fraction per circling, wherein a cold pool sounding is defined as having  $\theta_v$ -gradient height less than 400 m (Touzé-Peiffer et al. 2022). The residual structure is, however, not correlated with these proxies. For WALES cloud top height, correlations are  $r = 0.19$  for  $\bar{q}$  residuals and  $r = 0.16$  for  $\bar{\theta}$  residuals. For the cold pool fraction, these correlations are also small,  $r = 0.23$  for  $\bar{q}$  residuals and  $r = 0.24$  for  $\bar{\theta}$  residuals. The weak correlations support our finding that the subcloud-layer moisture and heat budgets can close solely by representing small-scale entrainment mixing. These findings, that the influence of downdrafts and other coherent structures is relatively

small (at least in the trades) relative to turbulent entrainment mixing, are consistent with Thayer-Calder and Randall (2015), justifying assumptions in many parameterizations, dating back to Arakawa and Schubert (1974).

**6. How do these subcloud-layer properties relate to the large-scale environment?**

*a. Wind speed variability*

Figure 7 relates variability among  $\|U\|$ ,  $h$ , surface fluxes, entrainment fluxes, and the clear-sky radiative cooling  $Q_r$ . A deeper subcloud layer tends to be associated with stronger  $\|U\|$ ,  $r = 0.62$ , consistent with Nuijens and Stevens (2012), though there are outliers with intermediate wind speeds leading to the smallest and largest heights. Naumann et al. (2017) and Naumann et al. (2019) suggest that stronger radiative cooling is associated with a smaller  $h$ , while Zheng (2019) finds that stronger radiative cooling deepens the subcloud layer. Unfortunately, our observations do not allow us to resolve this discrepancy. We do not find a simple linear relationship between clear-sky radiative cooling and  $h$  (Fig. 7, bottom row) or mean thermodynamics. During the night, the wind speed tends to increase, deepening the subcloud layer, which could offset a decrease in the depth of this layer due to stronger nighttime radiative cooling. This compensation highlights the difficulty in disentangling the influence of clear-sky radiative cooling on subcloud-layer properties when its variability is aliased onto variability in other variables, such as the surface wind speed.

Surface and entrainment fluxes are strongly associated with  $\|U\|$  variability, as expected, given their structural dependence on the wind speed. Fixing other parameters at their campaign-mean value and only allowing  $\|U\|$  to change recovers most variance in surface and entrainment fluxes: 87% of the variance in  $F_q$ , 64% of the variance in  $E\Delta q$ , 74% of the variance in  $E\Delta\theta$ , though only 22% of the variance in  $F_\theta$ . If we instead allow only the sea surface temperature to vary, we recover 32% of the variance in  $F_q$ , 38% of the variance in  $E\Delta q$ , 11% of the variance in  $F_\theta$ , and 35% of the variance in  $E\Delta\theta$ . The surface wind speed plays a larger role in explaining variability in the fluxes except for  $F_\theta$ .

*b. Predictive skill of mixed-layer theory*

Having established that mixed-layer theory is a skillful framework (section 5), we can further employ it as a physical mapping to diagnose how boundary conditions, such as the surface wind speed, influence  $\bar{q}$  and  $\bar{\theta}$ . Solving for  $\bar{q}$  from Eq. (8) yields

$$\bar{q} = \frac{V_0 q_s + E q_+ - h \left( \frac{\partial q}{\partial t} + \mathbf{u} \cdot \nabla q \right)}{V_0 + E}. \tag{14}$$

Similarly, solving for  $\bar{\theta}$  from Eq. (9) yields

$$\bar{\theta} = \frac{V_0 \theta_s + E \theta_+ + h Q_r - h \left( \frac{\partial \theta}{\partial t} + \mathbf{u} \cdot \nabla \theta \right)}{V_0 + E}. \tag{15}$$

The velocity scale is  $V_0 = C_d \|U\|$ , and  $q_+$  and  $\theta_+$  correspond to values 150 m above the subcloud-layer top,  $h$ , though

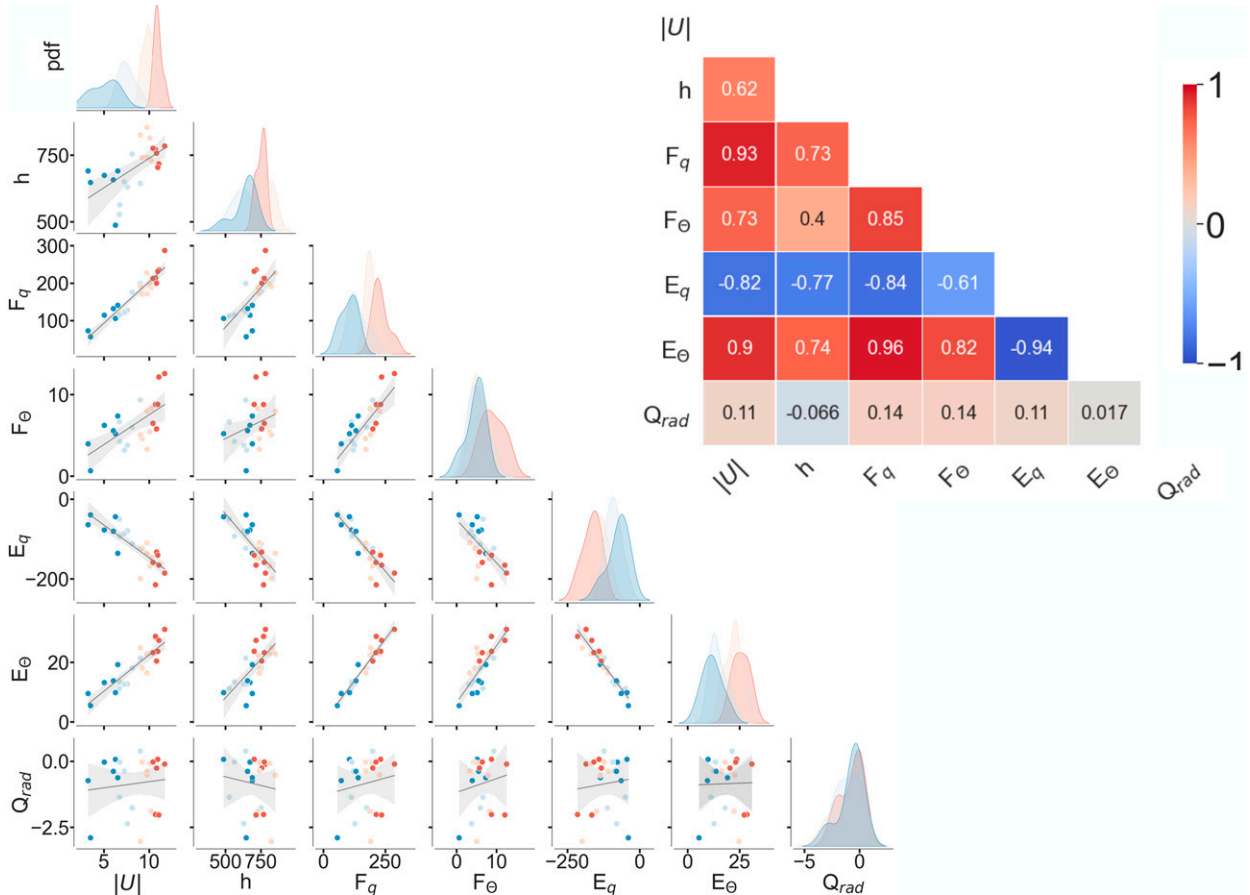


FIG. 7. Relationships among 10 m wind speed, subcloud-layer depth, surface fluxes, entrainment fluxes, and clear-sky radiative cooling. The black line is the ordinary least squares regression, and the gray shading is the 5%–95% confidence interval on the regression. Colors correspond to quartiles of the wind speed with increasing wind speed going from blue to red. Note that, along the diagonal, the probability density function (pdf) smooths the four distributions corresponding to quartiles of 10 m wind speed, though these quartiles are non-overlapping: (3.3–6.7], (6.7–9.0], (9.0–10.3], and (10.3–12]  $\text{m s}^{-1}$ . The inset shows the Pearson correlation coefficients among these variables.

results are similar for choosing any height between 100 and 500 m above  $h$ . The equation for  $E$  can, moreover, be rewritten as

$$E = \frac{A_e F_{\theta_v}}{\{\bar{\theta} + 0.61[\bar{\theta}(q_+ - \bar{q}) + \bar{q}(\theta_+ - \bar{\theta})]\} - \bar{\theta}_v}, \quad (16)$$

as function of  $q_+$  and  $\theta_+$ .

Predictions of  $\bar{q}$  from Eq. (14) recover 85% variance in observed  $\bar{q}$ , with a correlation coefficient  $r = 0.92$  (Fig. 8b). This simple theoretical framework thus has significant skill for predicting variability in mean subcloud-layer humidity. The simple framework has less skill for capturing variations in observed  $\bar{\theta}$ , with a correlation coefficient of  $r = 0.48$  between observed  $\bar{\theta}$  and  $\bar{\theta}$  calculated with Eq. (15). The weaker skill for potential temperature is qualitatively consistent with larger residuals in the heat budget. The reduced skill could result from multiple reasons: the smaller magnitude of variability in  $\bar{\theta}$  itself compared to  $\bar{q}$  (see Fig. 3), the smaller magnitude of the terms in the heat budget, and the presence of an additional term of radiative heating in the heat budget, wherein this radiative heating is here only

calculated as clear-sky following Albright et al. (2021). At times, there may be a substantial contribution from clouds, which is not accounted for in our analysis.

The success of Eq. (14) in explaining variability in  $\bar{q}$ , however, allows for exploring the influence of different boundary conditions on the mean subcloud-layer properties. We externalize different boundary conditions:  $|U|$ , SST,  $\mathbf{u} \cdot \nabla \bar{q}$ ,  $\mathbf{u} \cdot \nabla \bar{\theta}$ ,  $Q_r$ ,  $q_+$ ,  $\theta_+$ ,  $\partial q/\partial t$ , and  $\partial \theta/\partial t$ . The terms  $q_+$  and  $\theta_+$  are defined as the mean from  $h$  to  $h + 100$  m – that is, air just above the subcloud layer and within the cloud layer and may not be completely independent of the properties of the subcloud layer. Cloud-layer moisture variability is likely influenced by processes in the free atmosphere, such as dry intrusions (e.g., Stevens et al. 2021; Villiger et al. 2022).

To test the influence of these conditions, we vary one parameter at a time and fix the other parameters at their campaign-mean value to predict  $\bar{q}$  or  $\bar{\theta}$  values. Perhaps surprisingly, varying only the surface wind speed to predict  $\bar{q}$  yields a weak correlation with observed  $\bar{q}$  ( $r = -0.2$ ) or with predicted  $\bar{q}$  when allowing all external factors to vary ( $r = -0.11$ ), not only the wind. That the net influence of the wind speed is weak might seem to contradict

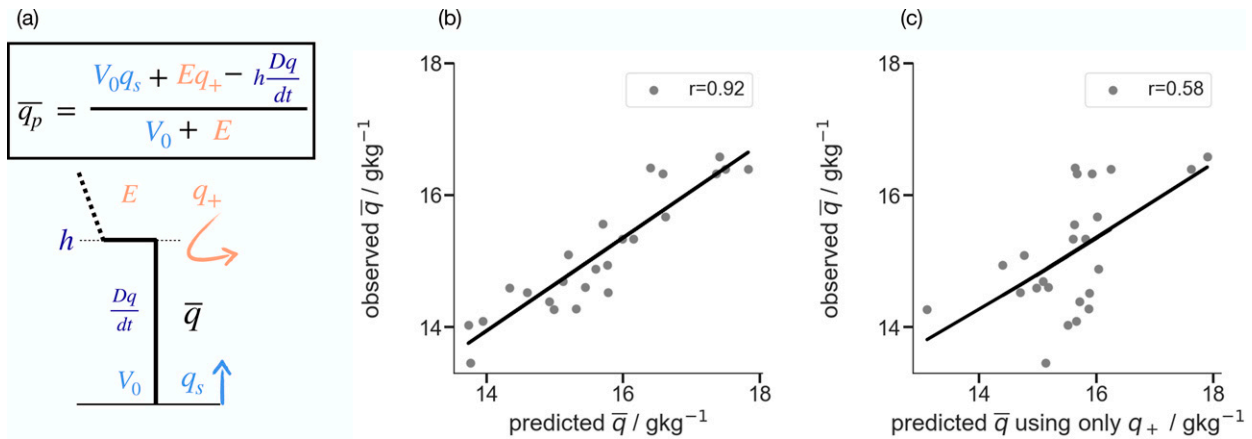


FIG. 8. (a) Schematic showing the factors influencing mean subcloud-layer specific humidity  $\bar{q}$ :  $V_0$  denotes the surface velocity scale, defined as  $C_d$  times the 10 m wind speed;  $h$  is the subcloud-layer height;  $q_s$  is the surface (saturated) specific humidity;  $E$  is the entrainment rate;  $q_+$  is defined as the mean from  $h$  to  $h + 100$  m; and  $Dq/dt$  is the total derivative of subcloud-layer mean specific humidity. (b) Scatterplot between  $\bar{q}$  predicted using Eq. (14) and observed  $\bar{q}$ , with linear regression and Pearson correlation coefficient. (c) Scatterplot between  $\bar{q}$  predicted using Eq. (14), but only allowing  $q_+$  to vary and keeping all other terms fixed at their campaign mean, and observed  $\bar{q}$ , with linear regression and Pearson correlation coefficient.

the previous discussion, but results from its opposing influences, both moistening the layer through surface fluxes and drying it through entrainment. Whereas the correlation of the surface wind speed with individual fluxes is strong (Fig. 7), the correlation of the wind speed with the sum of the surface moistening flux and entrainment drying flux is weak ( $r = 0.32$ ). Varying only  $q_+$ , which also influences the entrainment rate through  $\Delta\theta_v$ , yields the highest correlation with predicted moisture ( $r = 0.55$ ) and observed moisture ( $r = 0.58$ , Fig. 8c). For heat, we find that  $\theta_+$  has a correlation of  $r = 0.36$  with predicted  $\theta$  and  $r = 0.85$  with observed  $\theta$ .

In summary, variability in the fluxes is strongly influenced by  $\|U\|$  variability. Yet due to opposing influences of the surface and entrainment fluxes on  $\bar{q}$ , the surface wind speed does not strongly influence  $\bar{q}$  variability. Instead, knowing the humidity above the subcloud layer,  $q_+$ , is the most informative for reconstructing  $\bar{q}$  variability. Clouds, however, couple subcloud-layer moisture,  $\bar{q}$  and  $q_+$ , in which case it is difficult to infer causality. The strong predictive skill of  $q_+$  does point to the importance of understanding what controls dry intrusions into the cloud layer, such as extratropical dry intrusions discussed in Villiger et al. (2022), which can influence the subcloud-layer moisture by entraining relatively drier air from the layer above.

### 7. Conclusions

In this analysis, we quantify thermodynamic variability in the trade wind subcloud layer and test mixed-layer theory using extensive in situ observations from the EUREC<sup>4</sup>A campaign.

A primary question motivating our analyses is whether mixed-layer theory, as a simple and often-employed theoretical framework, is an appropriate and useful way to study how and why the subcloud layer varies. Regarding its appropriateness, a first assumption is that the subcloud layer is well-mixed vertically, and we find that vertical gradients, at least over the mixed layer, are small relative to variability about the mean (Fig. B1). Regarding

a second assumption about a “jump” at the subcloud-layer top, in defining the subcloud-layer height, we find evidence for a transition layer that separates the mixed-layer top from the subcloud-layer top (Fig. 2). The transition layer exhibits vertical gradients over finite thickness. The presence of the transition layer and its vertical gradients introduces ambiguity into the application of mixed-layer theory, in particular regarding the formulation of the entrainment rate and entrainment fluxes.

We address this uncertainty through the introduction of effective parameters related to entrainment, which are estimated using a Bayesian methodology. The mean effective entrainment efficiency,  $A_e = 0.43$  (Fig. 5), is greater than the value of 0.2 as often assumed. Such a large value of  $A_e$  is inconsistent with large eddy simulation (Fedorovich et al. 2004) and direct numerical simulation studies (Garcia and Mellado 2014) of idealized convective boundary layers. A large  $A_e$  value could arise if other processes are contributing to the energetics of mixing, for instance wind shear, cloud processes, or radiative cooling, or if the depth of the layer is taken to be too deep as compared to the height where the minimum buoyancy flux locates (e.g., Fedorovich et al. 2004; Canut et al. 2012). Applying our inversion technique using the shallower mixed-layer depth to specify  $h$  does not, however, resolve this discrepancy, nor does wind shear appear to play a role (see Fig. B2). This discrepancy leaves a possible disagreement with idealized simulations, or other processes, such as contributions from shallow clouds or radiative cooling in the transition layers, as candidate explanations for a larger  $A_e$ . Related to these considerations, there are other open questions regarding the transition layer that we address in a forthcoming publication, particularly, which physical processes give rise to its vertical structure.

Having accounted for the challenges that the transition layer posed for the formulation of entrainment in this theoretical framework, we find that mixed-layer theory can explain both synoptic and monthly mean variability in subcloud-layer moisture



and heat budgets, with campaign-residuals of  $3.6 \text{ W m}^{-2}$  for moisture and  $2.9 \text{ W m}^{-2}$  for heat. For synoptic variability across the campaign, the residuals are generally small and unbiased – that is, with uncertainties estimates crossing zero (Fig. 6). That the budgets close to within these small residuals suggests that knowledge of the mean state through  $\bar{q}$ ,  $\bar{\theta}$ , and  $h$  is generally sufficient to close the thermodynamic budgets, without having to include vertical thermodynamic gradients. We also find little evidence that closing moisture and heat budgets requires representing additional processes, such as precipitation or coherent downdrafts, and we can therefore not distinguish residuals from uncorrelated observational error.

After showing that mixed-layer theory is a skillful framework, we use this theory as a mapping between external conditions and subcloud-layer thermodynamics. In section 3c, we showed that  $\bar{q}$  varies significantly day-to-day and de-correlates after about 2 days, such that EUREC<sup>4</sup>A research flights sample nearly independent realizations of large-scale variability. Anomalies in the subcloud-layer depth and LCL are, moreover, largely associated with anomalies in  $\bar{q}$ . Given its large synoptic variability and influence on subcloud-layer vertical length scales, the primary mode of subcloud-layer thermodynamic variability therefore appears to be through  $\bar{q}$  variability, motivating our focus on  $\bar{q}$  variability. The simple mixed-layer theory framework is able to explain significant variability in observed  $\bar{q}$ , with a correlation  $r = 0.92$  between observed and predicted  $\bar{q}$  (Fig. 8b). Whereas we find strong linear relationships among variability in the surface wind speed and subcloud-layer depth, surface fluxes, and entrainment fluxes (Fig. 7), variability in the surface wind speed does not explain observed  $\bar{q}$  variability due to its compensating influences on both moistening the layer through surface fluxes and drying the layer through entrainment fluxes. Instead, only knowing moisture above the subcloud layer ( $q_+$ ) has the most predictive skill for variations in observed  $\bar{q}$  ( $r = 0.58$ , Fig. 8c) because these are the air masses that are incorporated into the subcloud layer by entrainment.

The ability of mixed-layer theory to observationally close subcloud-layer moisture and heat budgets gives confidence in using this approach to constrain trade cumulus feedbacks using the subcloud-layer mass budget, which is the focus of Vogel et al. (2022, manuscript submitted to *Nature*). In this work, mixed-layer theory, combined with novel sampling strategies, are used to perform the first process-level observational test to constrain trade cumulus feedbacks and climate sensitivity (e.g., Rieck et al. 2012; Zhang et al. 2013; Sherwood et al. 2014; Brient et al. 2016; Vial et al. 2016). Given the skill of the mixed-layer framework, it would also be worthwhile to apply this framework to representations of the trade wind subcloud layer by a hierarchy of models, from general circulation to storm-resolving models and large-eddy simulations. Variables analyzed could include subcloud-layer moisture or heat as in this study, momentum (e.g., Holland and Rasmusson 1973), or isotopes (e.g., Risi et al. 2020). Quantifying the relative magnitudes of different processes, how well the budgets close, and how individual terms vary according to large-scale environmental conditions would serve as a consistent framework for evaluating and comparing how well models represent physical processes, such as

surface and entrainment fluxes, relative to novel observational anchoring from the EUREC<sup>4</sup>A field campaign.

*Acknowledgments.* A.L.A., S.B., and R.V. gratefully acknowledge support from the European Research Council (ERC) under the European Union's Horizon 2020 research and innovation programme (EUREC<sup>4</sup>A Grant 694768). We thank Bruce Albrecht and an anonymous reviewer for their comments that improved our manuscript, and William Boos for his guidance in editing the manuscript. We also thank Kerry Emanuel, Geet George, Tobias Kölling, Marie Lothon, Theresa Mieslinger, and Jessica Vial for helpful discussions.

*Data availability statement.* JOANNE data are available at <https://doi.org/10.25326/246>. ATR-42 thermodynamic data are available at <https://doi.org/10.5194/essd-2021-459>. All EUREC<sup>4</sup>A data are also accessible at <https://observations.ipsl.fr/aeris/eurec4a-data/>. ERA5 data were accessed from the IPSL Prodiguer-Ciclad facility.

## APPENDIX A

### Methodology for Various Boundary and Subcloud-Layer Height Estimates

#### a. Thermodynamic variable gradient method

The vertical stratification of the tropical atmosphere occurs in all variables, but it is most evident in moisture (Augstein et al. 1974; Stevens et al. 2001). We first define a subcloud-layer length scale as the depth over which there is no vertical gradient in specific humidity within a threshold, applying the method from Canut et al. (2012). The method selects the height where the specific humidity becomes greater than the density-weighted mean specific humidity of the levels below by a certain threshold  $\epsilon_q: |q(z) - \bar{q}| \leq \epsilon_q$ , where  $\bar{q}$  is updated at each vertical level. We begin at a height of 100 m to minimize the influence of the surface layer. This humidity-jump approach was implicitly adopted in Malkus (1958), and is similar to previous estimates based on discontinuities in observed profiles (e.g., Heffter 1980; Marsik et al. 1995).

In implementing the  $q$ -gradient method, the primary uncertainty is the choice of threshold  $\epsilon_q$ , which should be large enough not to be biased by small-scale vertical variability, but precise enough to identify the humidity discontinuity at the subcloud-layer top. To choose a threshold, we turn to intensive sampling from both the CU-RAAVEN remotely piloted aircraft and the ATR-42 and HALO aircraft. Empirically, we choose a threshold that is one-third of turbulent, eddy-scale variability, estimated as within-flight variability (compared with day-to-day variability). Calculating the specific humidity standard deviation below 550 m within a 3-hourly flight of the CU-RAAVEN suggests a threshold  $\epsilon = 0.3 \text{ g kg}^{-1}$ . Calculating the standard deviation in  $q$  below 500 m from the ATR-42 yields a threshold  $\epsilon = 0.35 \text{ g kg}^{-1}$ , and for HALO soundings within one flight, one-third of the standard deviation is  $\epsilon = 0.27 \text{ g kg}^{-1}$ . We use the largest value,  $\epsilon = 0.35 \text{ g kg}^{-1}$ . The maximum allowable vertical gradient in the boundary

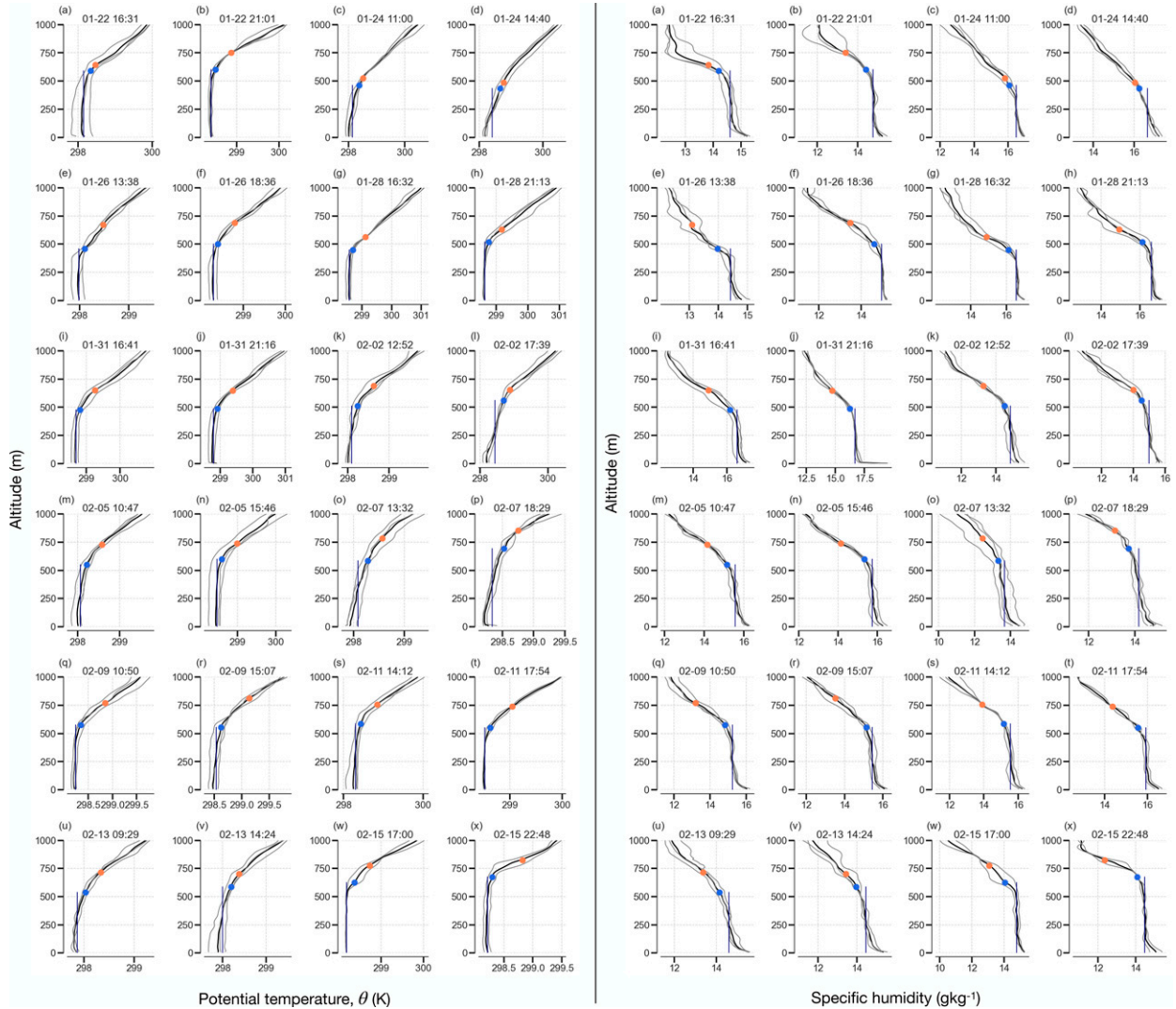


FIG. B1. The 24 circling-mean profiles (black: aggregate of about 36 dropsondes each) of (left) potential temperature  $\theta$  and (right) specific humidity  $q$ . Each panel also shows the three circle-mean profiles (gray) averaged to estimate each circling-mean. Blue dots correspond to the mixed-layer top, estimated with the  $q$ -gradient definition, and orange dots denote the subcloud-layer top, estimated with the  $\theta_v$ -gradient definition. The vertical navy line denotes the mixed-layer-mean value and demonstrates that the majority of profiles have a vertically well-mixed layer for thermodynamic variables.

layer is thus  $0.035 \text{ g kg}^{-1} \text{ m}^{-1}$ , given a 10 m grid spacing. This threshold allows for a certain moisture gradient, or deviation from a perfectly well-mixed profile, noted previously for both the trades and other environments (Malkus 1958; Mahrt 1976; Dai et al. 2014) and shown by our analyses. Across the HALO dropsonde soundings, this  $0.35 \text{ g kg}^{-1}$  threshold corresponds to a 10% difference between mean air in the cloud and subcloud layer, when averaging air masses between 1000–1200 and 100–300 m depths. We evaluate this height method and empirically chosen gradient in section 3. Heights from the  $q$ -gradient method are  $546 \pm 82 \text{ m}$ , with values denoting the mean and standard deviation across the 69 circle-mean data.

An advantage of this threshold definition is its straightforward application to other thermodynamic variables like  $\theta$  and  $\theta_v$ :  $|\theta(z) - \bar{\theta}| \geq \epsilon_\theta$ . We use thresholds 0.15 K for  $\theta$  and 0.20 K

for  $\theta_v$ . The threshold of 0.2 K for  $\theta_v$  is also employed in Touz -Peiffer et al. (2022). These thresholds are similarly chosen from the CU-RAAVEN, ATR-42, and HALO sounding data as one-third of one standard deviation within flights. These thresholds correspond to 10% of differences between cloud and boundary layer air (estimated conservatively as the 1000–1200 m minus 100–400 m layer-means) for  $\theta$  and  $\theta_v$ , respectively. Heights from the  $\theta$ -gradient are  $549 \pm 97 \text{ m}$  and  $697 \pm 94 \text{ m}$  for the  $\theta$ -gradient, with values denoting the mean and standard deviation across the 69 circle-mean data.

b. Parcel method

Next, we examine the parcel method, also referred to as the ‘‘Holzworth method,’’ as introduced by Holzworth (1964),

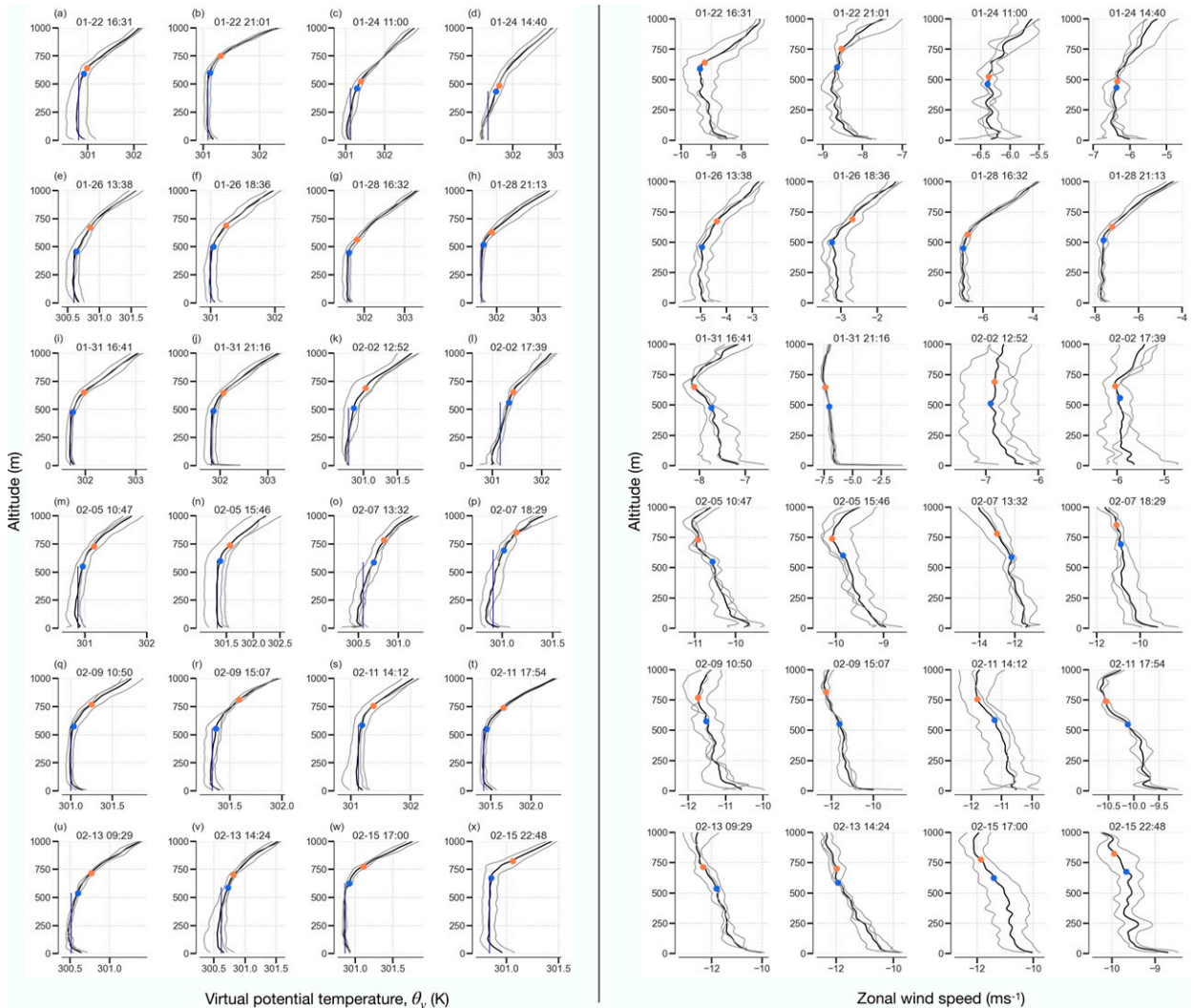


FIG. B2. The 24 circling-mean profiles (black, aggregate of about 36 dropsondes each) of (left) virtual potential temperature  $\theta_v$  and (right) zonal wind speed. Each panel also shows the three circle-mean profiles (gray) averaged to estimate each circling-mean. Blue dots correspond to the mixed-layer top, estimated with the  $q$ -gradient definition, and orange dots denote the subcloud-layer top, estimated with the  $\theta_v$ -gradient definition. The vertical navy line denotes the mixed-layer-mean value and demonstrates that the majority of profiles have a vertically well-mixed layer for thermodynamic variables (but not the wind speed).

which estimates the level at which a hypothetical rising parcel of surface air, representing a thermal, reaches its level of neutral buoyancy. We compute the level of neutral buoyancy where  $\theta_v$  surface parcels intersect a background profile fitted to the cloud-layer  $\theta_v$  profile determined by linear regression. Surface air is defined as 0–50 m values; choosing 0–90 m air affects the height by  $O(1\%)$ . We calculate the cloud-layer  $\theta_v$  profile from 100 m above the height determined from the  $q$ -gradient method to the first inversion-base height, defined where the static stability first exceeds  $0.1 \text{ K hPa}^{-1}$ , similar to a definition given in Bony and Stevens (2019).

This parcel method can be viewed as a simplification of the Richardson-number method that neglects the shear contribution (e.g., Seibert et al. 2000; Dai et al. 2014; Zhang et al. 2014). Although the Richardson and gradient Richardson number methods

are related to the generation and consumption of mixed-layer turbulence and diagnose flow stability (e.g., Garratt 1994; Stull 2012), we do not employ this method due to the considerable uncertainty underlying choices in its free parameters (e.g., Zilitinkevich and Baklanov 2002; Seidel et al. 2012). Heights from the parcel method are  $719 \pm 85 \text{ m}$ .

### c. Linearized relative humidity profile

A third type of definition involves the relative humidity profiles. The relative humidity increases throughout the subcloud layer (e.g., Nuijens et al. 2015), as the specific humidity  $q$  remains largely constant while temperature decreases. In practice, spurious peaks in relative humidity in our circle-mean profiles could arise from the spatial averaging of multiple soundings. For instance, a circle-mean could average between profiles falling



through a cloud close to the subcloud-layer top, saturated in relative humidity, and drier profiles elsewhere along the EUREC<sup>4</sup>A circle flight path.

To circumvent this bias, we introduce a linearization of the relative humidity profile. We find the first local maximum in relative humidity above 300 m and then linearize the relative humidity profile, by ordinary least squares regression, from 50 m above the surface to 50 m above this first local relative humidity maximum. We then find all local relative humidity maxima below 1 km and choose the height that minimizes the relative humidity difference between the observed and linearized profiles. Heights from the relative humidity maximum method are  $571 \pm 96$  m.

### APPENDIX B

#### Vertical Thermodynamic Profiles

To further illustrate the vertical structure as described in section 3, we show vertical profiles of potential temperature  $\theta$  and specific humidity  $q$  (Fig. B1), and vertical profiles of virtual potential temperature,  $\theta_v$ , and zonal wind speed (Fig. B2).

### APPENDIX C

#### Derivation for Entrainment Efficiency Parameter $A_e$

For a subcloud-layer scalar  $\vartheta$ , Eq. (13) results from integrating the following equation over a thin interfacial layer with lower and upper boundaries  $h_- = h - \epsilon$  and  $h_+ = h + \epsilon$  and layer-thickness  $\delta h = h_+ - h_- = 2\epsilon$ :

$$\int_{h_-}^{h_+} \frac{\partial \bar{\vartheta}}{\partial t} dz = - \int_{h_-}^{h_+} \frac{\partial}{\partial z} \overline{w' \vartheta'} dz. \quad (C1)$$

Applying the Leibniz integral rule for differentiation under integration yields

$$\frac{d}{dt} \left[ \langle \bar{\vartheta} \rangle_{\delta h} \delta h \right] - \frac{dh_+}{dt} \bar{\vartheta}_{h_+} + \frac{dh_-}{dt} \bar{\vartheta}_{h_-} = - \overline{w' \vartheta'}|_{h_+} + \overline{w' \vartheta'}|_{h_-}. \quad (C2)$$

Assuming that turbulence vanishes at  $h_+$  implies that  $\overline{w' \vartheta'}|_{h_+} = 0$ . Heights  $h_+$  and  $h_-$  are offset from  $h$  by a constant  $\epsilon$  such that  $h_+ = h + \epsilon$  and  $h_- = h - \epsilon$ , which means that  $dh_+/dt = dh_-/dt = dh/dt$ . Assuming that the layer is well-mixed implies that  $q_{h_-} = \bar{q}$ . With these assumptions, Eq. (C2) becomes

$$\frac{d}{dt} \left( \langle \bar{\vartheta} \rangle_{\delta h} \delta h \right) - \frac{dh}{dt} \Delta \vartheta = \overline{w' \vartheta'}|_{h_-}. \quad (C3)$$

If  $\delta h$  is constant and  $\langle \bar{\vartheta} \rangle_{\delta h}$  is approximately equal to  $(\bar{\vartheta} + \vartheta_+)/2$ , with  $\bar{\vartheta}$  equaling the mixed-layer mean value then Eq. (C3) becomes

$$\frac{\delta h}{2} \left( \frac{d\bar{\vartheta}}{dt} + \frac{d\vartheta_+}{dt} \right) - \frac{dh}{dt} \Delta \vartheta = \overline{w' \vartheta'}|_{h_-}. \quad (C4)$$

Note that if assuming that the interfacial layer has zero-thickness, e.g.,  $\delta h = 0$ , Eq. (C4) becomes

$$- \frac{dh}{dt} \Delta \vartheta = - E \Delta \vartheta = \overline{w' \vartheta'}|_{h_-}, \quad (C5)$$

where the growth of the layer  $dh/dt$  is considered the entrainment rate  $E$ .

Replacing  $\vartheta$  with  $\theta_v$  yields Eq. (13):

$$\frac{\delta h}{2} \left[ \frac{d\bar{\theta}_v}{dt} + \frac{d\theta_{v+}}{dt} \right] - \frac{dh}{dt} \Delta \theta_v = \overline{w' \theta'_v}|_{h_-}. \quad (C6)$$

Rearranging to solve for  $E = dh/dt$  yields and adopting the formulation for the flux,  $w' \theta'_v|_{h_-}$ , given in Eq. (2) and Eq. (4) yields

$$E = \frac{-AV_0 \Delta_0 \theta_v}{\Delta_1 \theta_v} + \frac{\delta h}{2 \Delta_1 \theta_v} \left( \frac{d\bar{\theta}_v}{dt} + \frac{d\theta_{v+}}{dt} \right). \quad (C7)$$

The effective  $A_e$  can be interpreted as absorbing the second term on the right-hand side in Eq. (C7).

### REFERENCES

- Albrecht, B. A., A. K. Betts, W. H. Schubert, and S. K. Cox, 1979: Model of the thermodynamic structure of the trade-wind boundary layer: Part I. Theoretical formulation and sensitivity tests. *J. Atmos. Sci.*, **36**, 73–89, [https://doi.org/10.1175/1520-0469\(1979\)036<0073:MOTTSSO>2.0.CO;2](https://doi.org/10.1175/1520-0469(1979)036<0073:MOTTSSO>2.0.CO;2).
- Albright, A. L., B. Fildier, L. Touz -Peiffer, R. Pincus, J. Vial, and C. Muller, 2021: Atmospheric radiative profiles during EUREC<sup>4</sup>A. *Earth Syst. Sci. Data*, **13**, 617–630, <https://doi.org/10.5194/essd-13-617-2021>.
- Arakawa, A., and W. H. Schubert, 1974: Interaction of a cumulus cloud ensemble with the large-scale environment, Part I. *J. Atmos. Sci.*, **31**, 674–701, [https://doi.org/10.1175/1520-0469\(1974\)031<0674:IOACCE>2.0.CO;2](https://doi.org/10.1175/1520-0469(1974)031<0674:IOACCE>2.0.CO;2).
- Augstein, E., H. Riehl, F. Ostapoff, and V. Wagner, 1973: Mass and energy transports in an undisturbed Atlantic trade-wind flow. *Mon. Wea. Rev.*, **101**, 101–111, [https://doi.org/10.1175/1520-0493\(1973\)101<0101:MAETIA>2.3.CO;2](https://doi.org/10.1175/1520-0493(1973)101<0101:MAETIA>2.3.CO;2).
- , H. Schmidt, and F. Ostapoff, 1974: The vertical structure of the atmospheric planetary boundary layer in undisturbed trade winds over the Atlantic Ocean. *Bound.-Layer Meteor.*, **6**, 129–150, <https://doi.org/10.1007/BF00232480>.
- Bellon, G., and B. Stevens, 2012: Using the sensitivity of large-eddy simulations to evaluate atmospheric boundary layer models. *J. Atmos. Sci.*, **69**, 1582–1601, <https://doi.org/10.1175/JAS-D-11-0160.1>.
- , and —, 2013: Time scales of the trade wind boundary layer adjustment. *J. Atmos. Sci.*, **70**, 1071–1083, <https://doi.org/10.1175/JAS-D-12-0219.1>.
- Betts, A. K., 1976: Modeling subcloud layer structure and interaction with shallow cumulus layer. *J. Atmos. Sci.*, **33**, 2363–2382, [https://doi.org/10.1175/1520-0469\(1976\)033<2363:MSLSAI>2.0.CO;2](https://doi.org/10.1175/1520-0469(1976)033<2363:MSLSAI>2.0.CO;2).
- , and B. A. Albrecht, 1987: Conserved variable analysis of the convective boundary layer thermodynamic structure over the tropical oceans. *J. Atmos. Sci.*, **44**, 83–99, [https://doi.org/10.1175/1520-0469\(1987\)044<0083:CVAOTC>2.0.CO;2](https://doi.org/10.1175/1520-0469(1987)044<0083:CVAOTC>2.0.CO;2).
- , and W. Ridgway, 1989: Climatic equilibrium of the atmospheric convective boundary layer over a tropical ocean.



- J. Atmos. Sci.*, **46**, 2621–2641, [https://doi.org/10.1175/1520-0469\(1989\)046<2621:CEOTAC>2.0.CO;2](https://doi.org/10.1175/1520-0469(1989)046<2621:CEOTAC>2.0.CO;2).
- Beyrich, F., and J.-P. Leps, 2012: An operational mixing height data set from routine radiosoundings at Lindenberg: Methodology. *Meteor. Z.*, **21**, 337–348, <https://doi.org/10.1127/0941-2948/2012/0333>.
- Bigorre, S. P., and A. J. Plueddemann, 2021: The annual cycle of air-sea fluxes in the northwest tropical Atlantic. *Front. Mar. Sci.*, **7**, 612842, <https://doi.org/10.3389/fmars.2020.612842>.
- Bock, O., P. Bossler, C. Flamant, E. Doerflinger, F. Jansen, R. Fages, S. Bony, and S. Schnitt, 2021: Integrated water vapour observations in the Caribbean arc from a network of ground-based GNSS receivers during EUREC<sup>4</sup>A. *Earth Syst. Sci. Data*, **13**, 2407–2436, <https://doi.org/10.5194/essd-13-2407-2021>.
- Bony, S., and J.-L. Dufresne, 2005: Marine boundary layer clouds at the heart of tropical cloud feedback uncertainties in climate models. *Geophys. Res. Lett.*, **32**, L20806, <https://doi.org/10.1029/2005GL023851>.
- , and B. Stevens, 2019: Measuring area-averaged vertical motions with dropsondes. *J. Atmos. Sci.*, **76**, 767–783, <https://doi.org/10.1175/JAS-D-18-0141.1>.
- , J.-L. Dufresne, H. Le Treut, J.-J. Morcrette, and C. Senior, 2004: On dynamic and thermodynamic components of cloud changes. *Climate Dyn.*, **22**, 71–86, <https://doi.org/10.1007/s00382-003-0369-6>.
- , and Coauthors, 2017: EUREC<sup>4</sup>A: A field campaign to elucidate the couplings between clouds, convection and circulation. *Surv. Geophys.*, **38**, 1529–1568, <https://doi.org/10.1007/s10712-017-9428-0>.
- , and Coauthors, 2022: EUREC<sup>4</sup>A observations from the SAFIRE ATR42 aircraft. *Earth Syst. Sci. Data*, **14**, 2021–2064, <https://doi.org/10.5194/essd-14-2021-2022>.
- Bretherton, C. S., and Coauthors, 1999: An intercomparison of radiatively driven entrainment and turbulence in a smoke cloud, as simulated by different numerical models. *Quart. J. Roy. Meteor. Soc.*, **125**, 391–423, <https://doi.org/10.1002/qj.49712555402>.
- Brient, F., T. Schneider, Z. Tan, S. Bony, X. Qu, and A. Hall, 2016: Shallowness of tropical low clouds as a predictor of climate models' response to warming. *Climate Dyn.*, **47**, 433–449, <https://doi.org/10.1007/s00382-015-2846-0>.
- Caldwell, P., C. S. Bretherton, and R. Wood, 2005: Mixed-layer budget analysis of the diurnal cycle of entrainment in southeast Pacific stratocumulus. *J. Atmos. Sci.*, **62**, 3775–3791, <https://doi.org/10.1175/JAS3561.1>.
- Canut, G., F. Couvreux, M. Lohon, D. Pino, and F. Saïd, 2012: Observations and large-eddy simulations of entrainment in the sheared Sahelian boundary layer. *Bound.-Layer Meteor.*, **142**, 79–101, <https://doi.org/10.1007/s10546-011-9661-x>.
- Chazette, P., F. Marnas, J. Totems, and X. Shang, 2014: Comparison of IASI water vapor retrieval with H<sub>2</sub>O-Raman lidar in the framework of the Mediterranean HyMeX and ChArMEx programs. *Atmos. Chem. Phys.*, **14**, 9583–9596, <https://doi.org/10.5194/acp-14-9583-2014>.
- Dai, C., Q. Wang, J. Kalogiros, D. Lenschow, Z. Gao, and M. Zhou, 2014: Determining boundary-layer height from aircraft measurements. *Bound.-Layer Meteor.*, **152**, 277–302, <https://doi.org/10.1007/s10546-014-9929-z>.
- De Boer, G., and Coauthors, 2022: Measurements from the University of Colorado RAAVEN uncrewed aircraft system during ATOMIC. *Earth Syst. Sci. Data*, **14**, 19–31, <https://doi.org/10.5194/essd-14-19-2022>.
- Deardorff, J. W., 1972: Parameterization of the planetary boundary layer for use in general circulation models. *Mon. Wea. Rev.*, **100**, 93–106, [https://doi.org/10.1175/1520-0493\(1972\)100<0093:POTPBL>2.3.CO;2](https://doi.org/10.1175/1520-0493(1972)100<0093:POTPBL>2.3.CO;2).
- Driedonks, A., 1982: Models and observations of the growth of the atmospheric boundary layer. *Bound.-Layer Meteor.*, **23**, 283–306, <https://doi.org/10.1007/BF00121117>.
- Emanuel, K. A., 1986: An air-sea interaction theory for tropical cyclones. Part I: Steady-state maintenance. *J. Atmos. Sci.*, **43**, 585–605, [https://doi.org/10.1175/1520-0469\(1986\)043<0585:AASITF>2.0.CO;2](https://doi.org/10.1175/1520-0469(1986)043<0585:AASITF>2.0.CO;2).
- , 1993: The effect of convective response time on WISHE modes. *J. Atmos. Sci.*, **50**, 1763–1776, [https://doi.org/10.1175/1520-0469\(1993\)050<1763:TEOCRT>2.0.CO;2](https://doi.org/10.1175/1520-0469(1993)050<1763:TEOCRT>2.0.CO;2).
- Fairall, C. W., E. F. Bradley, J. Hare, A. A. Grachev, and J. B. Edson, 2003: Bulk parameterization of air–sea fluxes: Updates and verification for the COARE algorithm. *J. Climate*, **16**, 571–591, [https://doi.org/10.1175/1520-0442\(2003\)016<0571:BPOASF>2.0.CO;2](https://doi.org/10.1175/1520-0442(2003)016<0571:BPOASF>2.0.CO;2).
- Fedorovich, E., R. Conzemius, and D. Mironov, 2004: Convective entrainment into a shear-free, linearly stratified atmosphere: Bulk models reevaluated through large eddy simulations. *J. Atmos. Sci.*, **61**, 281–295, [https://doi.org/10.1175/1520-0469\(2004\)061<0281:CEIASL>2.0.CO;2](https://doi.org/10.1175/1520-0469(2004)061<0281:CEIASL>2.0.CO;2).
- Garcia, J. R., and J. P. Mellado, 2014: The two-layer structure of the entrainment zone in the convective boundary layer. *J. Atmos. Sci.*, **71**, 1935–1955, <https://doi.org/10.1175/JAS-D-13-0148.1>.
- Garratt, J. R., 1994: The atmospheric boundary layer. *Earth-Sci. Rev.*, **37**, 89–134, [https://doi.org/10.1016/0012-8252\(94\)90026-4](https://doi.org/10.1016/0012-8252(94)90026-4).
- Garstang, M., and Coauthors, 2019: Three early tropical field experiments. *Bull. Amer. Meteor. Soc.*, **100**, 2243–2258, <https://doi.org/10.1175/BAMS-D-18-0151.1>.
- George, G., and Coauthors, 2021: JOANNE: Joint dropsonde observations of the atmosphere in tropical North Atlantic meso-scale environments. *Earth Syst. Sci. Data*, **13**, 5253–5272, <https://doi.org/10.5194/essd-13-5253-2021>.
- Ghate, V. P., D. B. Mechem, M. P. Cadeddu, E. W. Eloranta, M. P. Jensen, M. L. Nordeen, and W. L. Smith Jr., 2019: Estimates of entrainment in closed cellular marine stratocumulus clouds from the MAGIC field campaign. *Quart. J. Roy. Meteor. Soc.*, **145**, 1589–1602, <https://doi.org/10.1002/qj.3514>.
- Hastings, W. K., 1970: Monte Carlo sampling methods using Markov chains and their application. *Biometrika*, **57**, 97–109, <https://doi.org/10.1093/biomet/57.1.97>.
- Heckley, W. A., 1985: Systematic errors of the ECMWF operational forecasting model in tropical regions. *Quart. J. Roy. Meteor. Soc.*, **111**, 709–738, <https://doi.org/10.1002/qj.49711146904>.
- Heffter, J. L., 1980: Air Resources Laboratories Atmospheric Transport and Dispersion Model (ARL-ATAD). Tech. Rep. NOAA-TM-ERL-ARL-81, 29 pp., <https://repository.library.noaa.gov/view/noaa/13189>.
- Hersbach, H., and Coauthors, 2020: The ERA5 global reanalysis. *Quart. J. Roy. Meteor. Soc.*, **146**, 1999–2049, <https://doi.org/10.1002/qj.3803>.
- Holland, J. Z., and E. M. Rasmusson, 1973: Measurements of the atmospheric mass, energy, and momentum budgets over a 500-kilometer square of tropical ocean. *Mon. Wea. Rev.*, **101**, 44–55, [https://doi.org/10.1175/1520-0493\(1973\)101<0044:MOTAME>2.3.CO;2](https://doi.org/10.1175/1520-0493(1973)101<0044:MOTAME>2.3.CO;2).
- Holzworth, G. C., 1964: Estimates of mean maximum mixing depths in the contiguous United States. *Mon. Wea. Rev.*,

- 92, 235–242, [https://doi.org/10.1175/1520-0493\(1964\)092<0235:EOMMMD>2.0.CO;2](https://doi.org/10.1175/1520-0493(1964)092<0235:EOMMMD>2.0.CO;2).
- Kalmus, P., M. Lebsock, and J. Teixeira, 2014: Observational boundary layer energy and water budgets of the stratocumulus-to-cumulus transition. *J. Climate*, **27**, 9155–9170, <https://doi.org/10.1175/JCLI-D-14-00242.1>.
- Kawa, S., and R. Pearson Jr., 1989: An observational study of stratocumulus entrainment and thermodynamics. *J. Atmos. Sci.*, **46**, 2649–2661, [https://doi.org/10.1175/1520-0469\(1989\)046<2649:AOSOSE>2.0.CO;2](https://doi.org/10.1175/1520-0469(1989)046<2649:AOSOSE>2.0.CO;2).
- Konow, H., and Coauthors, 2021: EUREC<sup>4</sup>A'S halo. *Earth Syst. Sci. Data*, **13**, 5545–5563, <https://doi.org/10.5194/essd-13-5545-2021>.
- Kraus, E. B., 1963: The diurnal precipitation change over the sea. *J. Atmos. Sci.*, **20**, 551–556, [https://doi.org/10.1175/1520-0469\(1963\)020<0551:TDPOT>2.0.CO;2](https://doi.org/10.1175/1520-0469(1963)020<0551:TDPOT>2.0.CO;2).
- LeMone, M. A., and W. T. Pennell, 1976: The relationship of trade wind cumulus distribution to subcloud layer fluxes and structure. *Mon. Wea. Rev.*, **104**, 524–539, [https://doi.org/10.1175/1520-0493\(1976\)104<0524:TROTWC>2.0.CO;2](https://doi.org/10.1175/1520-0493(1976)104<0524:TROTWC>2.0.CO;2).
- Lenschow, D. H., P. B. Krummel, and S. T. Siems, 1999: Measuring entrainment, divergence, and vorticity on the mesoscale from aircraft. *J. Atmos. Oceanic Technol.*, **16**, 1384–1400, [https://doi.org/10.1175/1520-0426\(1999\)016<1384:MEDAVO>2.0.CO;2](https://doi.org/10.1175/1520-0426(1999)016<1384:MEDAVO>2.0.CO;2).
- Lilly, D. K., 1968: Models of cloud-topped mixed layers under a strong inversion. *Quart. J. Roy. Meteor. Soc.*, **94**, 292–309, <https://doi.org/10.1002/qj.49709440106>.
- Liu, S., and X.-Z. Liang, 2010: Observed diurnal cycle climatology of planetary boundary layer height. *J. Climate*, **23**, 5790–5809, <https://doi.org/10.1175/2010JCLI3552.1>.
- Maddy, E. S., and C. D. Barnet, 2008: Vertical resolution estimates in version 5 of AIRS operational retrievals. *IEEE Trans. Geosci. Remote Sens.*, **46**, 2375–2384, <https://doi.org/10.1109/TGRS.2008.917498>.
- Mahrt, L., 1976: Mixed layer moisture structure. *Mon. Wea. Rev.*, **104**, 1403–1407, [https://doi.org/10.1175/1520-0493\(1976\)104<1403:MLMS>2.0.CO;2](https://doi.org/10.1175/1520-0493(1976)104<1403:MLMS>2.0.CO;2).
- Malkus, J. S., 1958: On the structure of the trade wind moist layer. *Phys. Oceanogr. Meteor.*, **13**, 1–48.
- Marsik, F. J., K. W. Fischer, T. D. McDonald, and P. J. Samson, 1995: Comparison of methods for estimating mixing height used during the 1992 Atlanta field intensive. *J. Appl. Meteor.*, **34**, 1802–1814, [https://doi.org/10.1175/1520-0450\(1995\)034<1802:COMFEM>2.0.CO;2](https://doi.org/10.1175/1520-0450(1995)034<1802:COMFEM>2.0.CO;2).
- McGauley, M., C. Zhang, and N. A. Bond, 2004: Large-scale characteristics of the atmospheric boundary layer in the eastern Pacific cold tongue–ITCZ region. *J. Climate*, **17**, 3907–3920, [https://doi.org/10.1175/1520-0442\(2004\)017<3907:LCOTAB>2.0.CO;2](https://doi.org/10.1175/1520-0442(2004)017<3907:LCOTAB>2.0.CO;2).
- Medeiros, B., and L. Nuijens, 2016: Clouds at Barbados are representative of clouds across the trade wind regions in observations and climate models. *Proc. Natl. Acad. Sci. USA*, **113**, E3062–E3070, <https://doi.org/10.1073/pnas.1521494113>.
- Metropolis, N., A. Rosenbluth, M. Rosenbluth, A. Teller, and E. Teller, 1953: Equation of state calculations by fast computing machines. *J. Chem. Phys.*, **21**, 1087–1092, <https://doi.org/10.1063/1.1699114>.
- Miller, R., 1997: Tropical thermostats and low cloud cover. *J. Climate*, **10**, 409–440, [https://doi.org/10.1175/1520-0442\(1997\)010<0409:TTALCC>2.0.CO;2](https://doi.org/10.1175/1520-0442(1997)010<0409:TTALCC>2.0.CO;2).
- Moeng, C.-H., P. P. Sullivan, and B. Stevens, 1999: Including radiative effects in an entrainment rate formula for buoyancy-driven PBLs. *J. Atmos. Sci.*, **56**, 1031–1049, [https://doi.org/10.1175/1520-0469\(1999\)056<1031:IREIAE>2.0.CO;2](https://doi.org/10.1175/1520-0469(1999)056<1031:IREIAE>2.0.CO;2).
- Myers, T. A., R. C. Scott, M. D. Zelinka, S. A. Klein, J. R. Norris, and P. M. Caldwell, 2021: Observational constraints on low cloud feedback reduce uncertainty of climate sensitivity. *Nat. Climate Change*, **11**, 501–507, <https://doi.org/10.1038/s41558-021-01039-0>.
- Naumann, A. K., B. Stevens, C. Hohenegger, and J. P. Mellado, 2017: A conceptual model of a shallow circulation induced by prescribed low-level radiative cooling. *J. Atmos. Sci.*, **74**, 3129–3144, <https://doi.org/10.1175/JAS-D-17-0030.1>.
- , —, and —, 2019: A moist conceptual model for the boundary layer structure and radiatively driven shallow circulations in the trades. *J. Atmos. Sci.*, **76**, 1289–1306, <https://doi.org/10.1175/JAS-D-18-0226.1>.
- Neggers, R., B. Stevens, and D. Neelin, 2006: A simple equilibrium model for shallow-cumulus-topped mixed layers. *Theor. Comput. Fluid Dyn.*, **20**, 305–322, <https://doi.org/10.1007/s00162-006-0030-1>.
- Nicholls, S., and M. A. Lemone, 1980: The fair weather boundary layer in GATE: The relationship of subcloud fluxes and structure to the distribution and enhancement of cumulus clouds. *J. Atmos. Sci.*, **37**, 2051–2067, [https://doi.org/10.1175/1520-0469\(1980\)037<2051:TFWBLL>2.0.CO;2](https://doi.org/10.1175/1520-0469(1980)037<2051:TFWBLL>2.0.CO;2).
- Nitta, T., and S. Esbensen, 1974: Heat and moisture budget analyses using BOMEX data. *Mon. Wea. Rev.*, **102**, 17–28, [https://doi.org/10.1175/1520-0493\(1974\)102<0017:HAMBAU>2.0.CO;2](https://doi.org/10.1175/1520-0493(1974)102<0017:HAMBAU>2.0.CO;2).
- Nuijens, L., and B. Stevens, 2012: The influence of wind speed on shallow marine cumulus convection. *J. Atmos. Sci.*, **69**, 168–184, <https://doi.org/10.1175/JAS-D-11-02.1>.
- , B. Medeiros, I. Sandu, and M. Ahlgrimm, 2015: Observed and modeled patterns of covariability between low-level cloudiness and the structure of the trade-wind layer. *J. Adv. Model. Earth Syst.*, **7**, 1741–1764, <https://doi.org/10.1002/2015MS000483>.
- Orlanski, I., 1975: A rational subdivision of scales for atmospheric processes. *Bull. Amer. Meteor. Soc.*, **56**, 527–530, <https://www.jstor.org/stable/26216020>.
- Pincus, R., A. Beljaars, S. A. Buehler, G. Kirchengast, F. Ladstaedter, and J. S. Whitaker, 2017: The representation of tropospheric water vapor over low-latitude oceans in (re-)analysis: Errors, impacts, and the ability to exploit current and prospective observations. *Surv. Geophys.*, **38**, 1399–1423, <https://doi.org/10.1007/s10712-017-9437-z>.
- Pino, D., J. V.-G. de Arellano, and P. G. Duynkerke, 2003: The contribution of shear to the evolution of a convective boundary layer. *J. Atmos. Sci.*, **60**, 1913–1926, [https://doi.org/10.1175/1520-0469\(2003\)060<1913:TCOSTT>2.0.CO;2](https://doi.org/10.1175/1520-0469(2003)060<1913:TCOSTT>2.0.CO;2).
- Rasp, S., H. Schulz, S. Bony, and B. Stevens, 2020: Combining crowdsourcing and deep learning to explore the mesoscale organization of shallow convection. *Bull. Amer. Meteor. Soc.*, **101**, E1980–E1995, <https://doi.org/10.1175/BAMS-D-19-0324.1>.
- Raymond, D. J., 1995: Regulation of moist convection over the west Pacific warm pool. *J. Atmos. Sci.*, **52**, 3945–3959, [https://doi.org/10.1175/1520-0469\(1995\)052<3945:ROMCOT>2.0.CO;2](https://doi.org/10.1175/1520-0469(1995)052<3945:ROMCOT>2.0.CO;2).
- Rieck, M., L. Nuijens, and B. Stevens, 2012: Marine boundary layer cloud feedbacks in a constant relative humidity atmosphere. *J. Atmos. Sci.*, **69**, 2538–2550, <https://doi.org/10.1175/JAS-D-11-0203.1>.
- Riehl, H., 1954: Variations of energy exchange between sea and air in the trades. *Weather*, **9**, 335–340, <https://doi.org/10.1002/j.1477-8696.1954.tb01706.x>.

- Risi, C., C. Muller, and P. Blossey, 2020: What controls the water vapor isotopic composition near the surface of tropical oceans? Results from an analytical model constrained by large-eddy simulations. *J. Adv. Model. Earth Syst.*, **12**, e2020MS002106. <https://doi.org/10.1029/2020MS002106>.
- Schalkwijk, J., H. J. Jonker, and A. P. Siebesma, 2013: Simple solutions to steady-state cumulus regimes in the convective boundary layer. *J. Atmos. Sci.*, **70**, 3656–3672. <https://doi.org/10.1175/JAS-D-12-0312.1>.
- Seibert, P., F. Beyrich, S.-E. Gryning, S. Joffre, A. Rasmussen, and P. Tercier, 2000: Review and intercomparison of operational methods for the determination of the mixing height. *Atmos. Environ.*, **34**, 1001–1027. [https://doi.org/10.1016/S1352-2310\(99\)00349-0](https://doi.org/10.1016/S1352-2310(99)00349-0).
- Seidel, D. J., Y. Zhang, A. Beljaars, J.-C. Golaz, A. R. Jacobson, and B. Medeiros, 2012: Climatology of the planetary boundary layer over the continental United States and Europe. *J. Geophys. Res.*, **117**, D17106. <https://doi.org/10.1029/2012JD018143>.
- Sherwood, S. C., S. Bony, and J.-L. Dufresne, 2014: Spread in model climate sensitivity traced to atmospheric convective mixing. *Nature*, **505**, 37–42. <https://doi.org/10.1038/nature12829>.
- Stevens, B., 2006: Bulk boundary-layer concepts for simplified models of tropical dynamics. *Theor. Comput. Fluid Dyn.*, **20**, 279–304. <https://doi.org/10.1007/s00162-006-0032-z>.
- , 2007: On the growth of layers of nonprecipitating cumulus convection. *J. Atmos. Sci.*, **64**, 2916–2931. <https://doi.org/10.1175/JAS3983.1>.
- , and Coauthors, 2001: Simulations of trade wind cumuli under a strong inversion. *J. Atmos. Sci.*, **58**, 1870–1891. [https://doi.org/10.1175/1520-0469\(2001\)058<1870:SOTWCU>2.0.CO;2](https://doi.org/10.1175/1520-0469(2001)058<1870:SOTWCU>2.0.CO;2).
- , J. Duan, J. C. McWilliams, M. Münnich, and J. D. Neelin, 2002: Entrainment, Rayleigh friction, and boundary layer winds over the tropical Pacific. *J. Climate*, **15**, 30–44. [https://doi.org/10.1175/1520-0442\(2002\)015<0030:ERFABL>2.0.CO;2](https://doi.org/10.1175/1520-0442(2002)015<0030:ERFABL>2.0.CO;2).
- , and Coauthors, 2003a: Dynamics and chemistry of marine stratocumulus—DYCOMS-II. *Bull. Amer. Meteor. Soc.*, **84**, 579–594. <https://doi.org/10.1175/BAMS-84-5-579>.
- , and Coauthors, 2003b: On entrainment rates in nocturnal marine stratocumulus. *Quart. J. Roy. Meteor. Soc.*, **129**, 3469–3493. <https://doi.org/10.1256/qj.02.202>.
- , and Coauthors, 2016: The Barbados cloud observatory: Anchoring investigations of clouds and circulation on the edge of the ITCZ. *Bull. Amer. Meteor. Soc.*, **97**, 787–801. <https://doi.org/10.1175/BAMS-D-14-00247.1>.
- , H. Brogniez, C. Kiemle, J.-L. Lacour, C. Crevoisier, and J. Kiliani, 2017: Structure and dynamical influence of water vapor in the lower tropical troposphere. *Surv. Geophys.*, **38**, 1371–1397. <https://doi.org/10.1007/s10712-017-9420-8>.
- , and Coauthors, 2021: EUREC<sup>4</sup>A. *Earth Syst. Sci. Data*, **13**, 4067–4119. <https://doi.org/10.5194/essd-13-4067-2021>.
- Stull, R. B., 1976: The energetics of entrainment across a density interface. *J. Atmos. Sci.*, **33**, 1260–1267. [https://doi.org/10.1175/1520-0469\(1976\)033<1260:TEOEAD>2.0.CO;2](https://doi.org/10.1175/1520-0469(1976)033<1260:TEOEAD>2.0.CO;2).
- , 2012: *An Introduction to Boundary Layer Meteorology*. Vol. 13, Springer Science and Business Media, 670 pp.
- Tennekes, H., 1973: A model for the dynamics of the inversion above a convective boundary layer. *J. Atmos. Sci.*, **30**, 558–567. [https://doi.org/10.1175/1520-0469\(1973\)030<0558:AMFTDO>2.0.CO;2](https://doi.org/10.1175/1520-0469(1973)030<0558:AMFTDO>2.0.CO;2).
- , and A. Driedonks, 1981: Basic entrainment equations for the atmospheric boundary layer. *Bound.-Layer Meteor.*, **20**, 515–531. <https://doi.org/10.1007/BF00122299>.
- Thayer-Calder, K., and D. Randall, 2015: A numerical investigation of boundary layer quasi-equilibrium. *Geophys. Res. Lett.*, **42**, 550–556. <https://doi.org/10.1002/2014GL062649>.
- Tiedtke, M., 1989: A comprehensive mass flux scheme for cumulus parameterization in large-scale models. *Mon. Wea. Rev.*, **117**, 1779–1800. [https://doi.org/10.1175/1520-0493\(1989\)117<1779:ACMFSF>2.0.CO;2](https://doi.org/10.1175/1520-0493(1989)117<1779:ACMFSF>2.0.CO;2).
- Touzé-Peiffer, L., R. Vogel, and N. Rochetin, 2022: Cold pools observed during EUREC<sup>4</sup>A: Detection and characterization from atmospheric soundings. *J. Appl. Meteor. Climatol.*, **61**, 593–610. <https://doi.org/10.1175/JAMC-D-21-0048.1>.
- Vaisala, 2022: Vaisala dropsonde RD41 datasheet. Vaisala, 2 pp., <https://www.vaisala.com/sites/default/files/documents/RD41-Datasheet-B211706EN.pdf>.
- van Zanten, M. C., P. G. Duynkerke, and J. W. Cuijpers, 1999: Entrainment parameterization in convective boundary layers. *J. Atmos. Sci.*, **56**, 813–828. [https://doi.org/10.1175/1520-0469\(1999\)056<0813:EPICBL>2.0.CO;2](https://doi.org/10.1175/1520-0469(1999)056<0813:EPICBL>2.0.CO;2).
- Vial, J., J.-L. Dufresne, and S. Bony, 2013: On the interpretation of inter-model spread in CMIP5 climate sensitivity estimates. *Climate Dyn.*, **41**, 3339–3362. <https://doi.org/10.1007/s00382-013-1725-9>.
- , S. Bony, J.-L. Dufresne, and R. Roehrig, 2016: Coupling between lower-tropospheric convective mixing and low-level clouds: Physical mechanisms and dependence on convection scheme. *J. Adv. Model. Earth Syst.*, **8**, 1892–1911. <https://doi.org/10.1002/2016MS000740>.
- Villiger, L., H. Wernli, M. Boettcher, M. Hagen, and F. Aemisegger, 2022: Lagrangian formation pathways of moist anomalies in the trade-wind region during the dry season: Two case studies from EUREC<sup>4</sup>A. *Wea. Climate Dyn.*, **3**, 59–88. <https://doi.org/10.5194/wcd-3-59-2022>.
- Vogel, R., S. Bony, and B. Stevens, 2020: Estimating the shallow convective mass flux from the subcloud-layer mass budget. *J. Atmos. Sci.*, **77**, 1559–1574. <https://doi.org/10.1175/JAS-D-19-0135.1>.
- Vömel, H., and Coauthors, 2021: High-resolution in situ observations of atmospheric thermodynamics using dropsondes during the Organization of Tropical East Pacific Convection (OTREC) field campaign. *Earth Syst. Sci. Data*, **13**, 1107–1117. <https://doi.org/10.5194/essd-13-1107-2021>.
- Webb, M. J., and Coauthors, 2006: On the contribution of local feedback mechanisms to the range of climate sensitivity in two GCM ensembles. *Climate Dyn.*, **27**, 17–38. <https://doi.org/10.1007/s00382-006-0111-2>.
- Wood, R., and C. S. Bretherton, 2004: Boundary layer depth, entrainment, and decoupling in the cloud-capped subtropical and tropical marine boundary layer. *J. Climate*, **17**, 3576–3588. [https://doi.org/10.1175/1520-0442\(2004\)017<3576:BLDEAD>2.0.CO;2](https://doi.org/10.1175/1520-0442(2004)017<3576:BLDEAD>2.0.CO;2).
- Yanai, M., S. Esbensen, and J.-H. Chu, 1973: Determination of bulk properties of tropical cloud clusters from large-scale heat and moisture budgets. *J. Atmos. Sci.*, **30**, 611–627. [https://doi.org/10.1175/1520-0469\(1973\)030<0611:DOBPOT>2.0.CO;2](https://doi.org/10.1175/1520-0469(1973)030<0611:DOBPOT>2.0.CO;2).
- Yin, B., and B. A. Albrecht, 2000: Spatial variability of atmospheric boundary layer structure over the eastern equatorial Pacific. *J. Climate*, **13**, 1574–1592. [https://doi.org/10.1175/1520-0442\(2000\)013<1574:SVOABL>2.0.CO;2](https://doi.org/10.1175/1520-0442(2000)013<1574:SVOABL>2.0.CO;2).
- Yu, L., R. A. Weller, and B. Sun, 2004: Mean and variability of the WHOI daily latent and sensible heat fluxes at in situ flux measurement sites in the Atlantic Ocean. *J. Climate*, **17**, 2096–2118. [https://doi.org/10.1175/1520-0442\(2004\)017<2096:MAVOTW>2.0.CO;2](https://doi.org/10.1175/1520-0442(2004)017<2096:MAVOTW>2.0.CO;2).

- Zhang, M., and Coauthors, 2013: CGILS: Results from the first phase of an international project to understand the physical mechanisms of low cloud feedbacks in single column models. *J. Adv. Model. Earth Syst.*, **5**, 826–842, <https://doi.org/10.1002/2013MS000246>.
- Zhang, Y., Z. Gao, D. Li, Y. Li, N. Zhang, X. Zhao, and J. Chen, 2014: On the computation of planetary boundary-layer height using the bulk Richardson number method. *Geosci. Model Dev.*, **7**, 2599–2611, <https://doi.org/10.5194/gmd-7-2599-2014>.
- Zheng, Y., 2019: Theoretical understanding of the linear relationship between convective updrafts and cloud-base height for shallow cumulus clouds. Part I: Maritime conditions. *J. Atmos. Sci.*, **76**, 2539–2558, <https://doi.org/10.1175/JAS-D-18-0323.1>.
- Zilitinkevich, S., and A. Baklanov, 2002: Calculation of the height of the stable boundary layer in practical applications. *Bound.-Layer Meteor.*, **105**, 389–409, <https://doi.org/10.1023/A:1020376832738>.